Towards an efficient numerical simulation of complex 3D knee joint motion [*]

Oliver Sander[1], Corinna Klapproth[2], Jonathan Youett[1], Ralf Kornhuber[1], and Peter Deuflhard[2]

[1] Freie Universität Berlin Institut für Mathematik, Arnimallee 6, D - 14195 Berlin, Germany
[2] Zuse Institute Berlin (ZIB), Takustraße 7, 14195 Berlin, Germany

Abstract. We present a time-dependent finite element model of the human knee joint of full 3D geometric complexity together with advanced numerical algorithms needed for its simulation. The model comprises bones, cartilage and the major ligaments, while patella and menisci are still missing. Bones are modeled by linear elastic materials, cartilage by linear viscoelastic materials, and ligaments by one-dimensional nonlinear Cosserat rods. In order to capture the dynamical contact problems correctly, we solve the full PDEs of elasticity with strict contact inequalities. The spatio–temporal discretization follows a time layers approach (first time, then space discretization). For the time discretization of the elastic and viscoelastic parts we use a new contact-stabilized Newmark method, while for the Cosserat rods we choose an energy–momentum method. For the space discretization, we use linear finite elements for the elastic and viscoelastic parts and novel geodesic finite elements for the Cosserat rods. The coupled system is solved by a Dirichlet–Neumann method. The large algebraic systems of the bone–cartilage contact problems are solved efficiently by the truncated non-smooth Newton multigrid method.

Key words biomechanics, time-dependent contact problem, contact-stabilized Newmark method, domain decomposition, energy-momentum method, geodesic finite elements, knee model

1 Introduction

It is an old dream of virtual medicine to accompany orthopaedic surgery by numerical simulations with the aim of finding optimal surgical strategies, in particular before a challenging intervention. To be of real help in practical surgery, detailed mathematical models are required. Such models have to include the full 3D geometry of individual patients as well as a full description of the dynamics of joint motion. The present paper attacks this challenging class of problems, focusing on the knee joint motion. Once this can be treated successfully, other joints will follow.

As early as 1986, simple models for the patello–femoral joint were suggested by van Eijden et al. [52] on the computational basis of multibody kinetics. These models, however, were insufficient in view of the above-mentioned medical purpose. Improved 2D multibody models were suggested by Abdel-Rahman and Hefzy [2] in 1999 and by Machado et al. [36] in 2010. In 2007 Heller et al. [20] introduced a modified four-bar linkage model that allows lengthening of the bars and internal/external rotation of the joint. Such models may certainly supply basic insight, but will not be reliable tools for backing patient-specific surgical decisions. For this reason, more complex 3D finite element (FE) models have been developed. In 2002, a static FE knee model was published by Donahue et al. [14], who performed a careful analysis based on three nested uniform FE meshes, the finest of which consisting of 14 050 hexahedral elements. As a substitute for a dynamical model, they studied a purely linear elastic model, ignoring the viscoelastic nature of the cartilage, under 10 steps of incremental boundary load going up to 800 N. In the same year, Penrose et al. [39] presented an FE knee model, which integrated the dynamics numerically by means of an explicit time integrator combined with a penalty function formulation, thus weakening the non-penetration condition at contact.

In one or the other way, these models failed to reliably model the dynamics. Furthermore, large computing times were needed despite the imposed simplifications (for example, 12–24 hours on an SGI Origin 2000 were reported in Penrose et al. [39]). That is probably why some later models used the computationally less challenging multibody framework again (see McLean et al. [37], who applied an explicit RK4 integrator, but did not include any contact model at all). In 2001, Piazza and Delp [40] presented a rather simple six-body segment model to capture the dynamics of the knee joint, but reported a rather poor consistency with measured data. In 2004, Bei and Fregly [9] suggested a combi-

nation of a multibody dynamics model with a spring model, a popular simplification for elasticity. For the arising differential equations of motion they applied the well-reputed implicit stiff integrator DASSL[1]. They presented a methodology for incorporating deformable contact models of the tibio–femoral joint into a multibody dynamics framework, which included the articular surface geometry, the calculation of distances between these surfaces, and a contact solver. However, such contact models within multibody approaches ignore the PDE structure of the problem. On the other hand, in [30,28] numerical methods were introduced that allowed the solution of small-strain contact problems as efficiently as linear problems and without any regularization parameters.

Besides complete joint models, the mathematical description of joint components like bones, ligaments, and cartilage has been investigated by many authors. For example, bone modeling often concentrates on the mathematical and computational challenges of the anisotropic multiscale nature of cortical and trabecular bone. We refer, e.g., to Ehlers [32] or Nackenhorst [38] who suggested biphasic or linearly elastic macroscopic models and to Arbenz [5] who derived numerical methods for microscopic descriptions.

The simplest models for ligaments consist of a single linear or nonlinear spring. They can be easily extended by using several springs representing different fibre bundles in each ligament. All these one-dimensional ligament models can only represent tensile stresses, and possibly contact stresses in some models (see, e.g., Blankevoort and Huiskes [10]). Yet, in reality ligaments also undergo some shear and transverse loading. As a natural representation of the resulting stresses, three-dimensional models have to be used (see, e.g., the survey article of Weiss and Gardiner [53]). Apart from computational complexity, large deformations of ligaments often cause severe numerical difficulties, e.g., with the construction of sufficiently regular meshes. This motivated various 2D simplifications, such as, e.g., shell models (see again Weiss and Gardiner [53] for details). Our approach to modeling of ligaments is carried out in the framework of Cosserat rods [4,43]. While retaining the advantages of a 1D model, they can express not only tension, but also large deformation shear, bending, and torsion.

There is a wide range of models for articular cartilage which differ in their representation of particular mechanical properties such as, e.g., swelling due to high negative charge density. Accounting for viscoelastic effects, biphasic approaches are often employed [21,51]. In order to incorporate the anisotropic structur of collagen fibres, so-called fibril-reinforced models have been derived [55]. Lai et al. [33] suggested a mechano-electrochemical triphasic model that also includes the influence of ion concentration within articular cartilage. We refer to the review article of Wilson et al. [54] for further details.

In spite of such a variety of models for different components like bones, ligaments, and cartilage, their assembly to heterogeneous 3D joint models has hardly been

tackled. A possible reason might be the computational complexity and the algorithmical challenges of the resulting nonlinear, non-smooth system of partial differential equations.

This is the general situation where the present paper starts off. The model we present aims at a patient-specific stress analysis, spatially resolved in full detail and including the dynamics of the time-dependent knee joint motion. The geometric model comprises the distal femur as well as the proximal tibia and fibula bones, with the articular surfaces being covered by layers of cartilage. Moreover, it contains cruciate and collateral ligaments.

We model bones as linearly elastic materials and cartilage as thin, but nevertheless three-dimensional layers of linearly viscoelastic Kelvin–Voigt materials. The contact between femur and tibia is formulated as a Signorini-type contact problem between two Kelvin–Voigt materials, where strict non-penetration is imposed. We assume a complete absence of friction.

The model here is an extension of the much simpler knee model presented earlier in [29]. While that model already incorporated fully dynamic bone–bone contact, the new model adds ligaments and viscoelastic articular cartilage. To emphasize the progression beyond [29], the numerical experiment to be shown at the end of this article is close to the one given there.

In its current state our model poses quite a few numerical challenges. We present a number of algorithms that have recently been developed and have separately been shown to be efficient on simpler test examples. We verify here that they work together efficiently when properly combined. On the discretization side, these new methods include a contact-stabilized Newmark method for the stable and reliable time discretization of dynamical contact problems, and geodesic finite elements for the intrinsic, frame-invariant discretization of Cosserat rod problems. For solving the discrete problems we combine a nonlinear Dirichlet–Neumann method for the coupled problem with the Truncated Nonsmooth Newton Multigrid (TNNMG) method for the contact problems.

The paper is organized as follows. In Section 2, we define the complete continuous, time-dependent, and heterogeneous knee model as a non-smooth PDE problem with strict inequalities and coupling constraints. In Section 3, we introduce time discretizations for the two different submodels. For bones and cartilage we apply the contact-stabilized Newmark integrator [27,24], whereas for Cosserat rods we select an energy–momentum method [50]. In Section 4, space discretizations for the various parts of the model are given. Bones and cartilage are discretized using first-order Lagrangian finite elements, and the contact conditions are treated with the mortar method. For the Cosserat rods, geodesic finite elements are used, which greatly simplify the overall discrete rod formulation, when compared to [50]. A fast solution algorithm for the coupled spatial problems is given in Section 5. This combines a Dirichlet–Neumann approach with a truncated non-smooth Newton multigrid methods [30,28]. Finally, in Section 6, we test our algorithms by repeating the
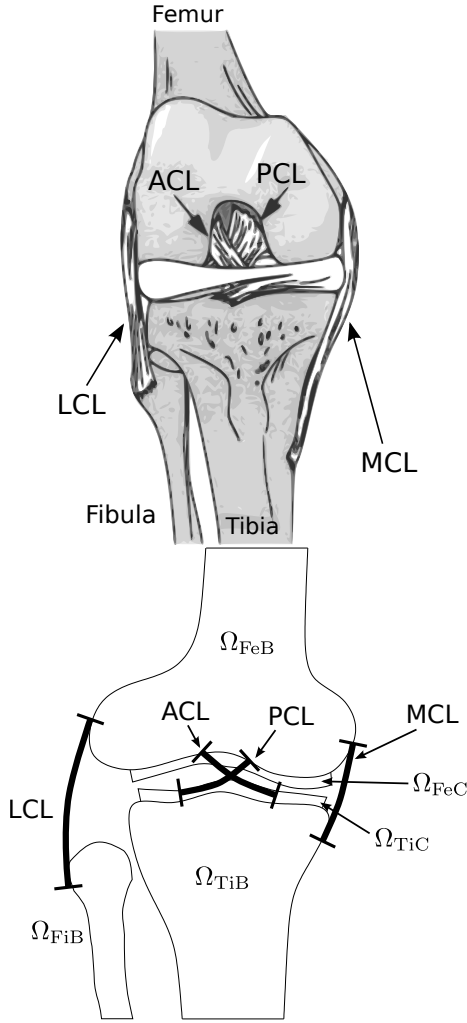
---

[1] `http://www.netlib.org/ode/ddassl.f`

Fig. 2.1. Upper: anatomy of a human knee joint (illustration taken from [53]). Lower: heterogeneous mathematical model. Note that the model includes cartilage layers, but not the menisci.

numerical experiment from [29] now with our improved model.

2 Continuous Time-Dependent Knee Model

We begin by introducing the time- and space-continuous knee model. The dynamics of the joint is modeled as a heterogeneous time-dependent contact problem. First we describe the mathematical model for bones and cartilage. Then we present a model for ligaments, and show how the two can be combined.

2.1 Bones and Cartilage

We consider a mechanical system consisting of three deformable continua, which model the distal femur, and the proximal tibia and fibula (Figure 2.1). With each of them we identify the closure of an open, connected domain in $\mathbb{R}^3$. These domains are supposed to be disjoint.

Ω_{FeB}	distal femur bone
Ω_{FeC}	cartilage on femur
$\Omega_{\text{Fe}} := \Omega_{\text{FeB}} \cup \Omega_{\text{FeC}}$	distal femur + cartilage
Ω_{TiB}	proximal tibia bone
Ω_{TiC}	cartilage on tibia
$\Omega_{\text{Ti}} := \Omega_{\text{TiB}} \cup \Omega_{\text{TiC}}$	proximal tibia + cartilage
Ω_{Fi}	proximal fibula
$\Omega_{\text{Bo}} := \Omega_{\text{FeB}} \cup \Omega_{\text{TiB}} \cup \Omega_{\text{FiB}}$	femur, tibia, and fibula bone
$\Omega_{\text{Ca}} := \Omega_{\text{FeC}} \cup \Omega_{\text{TiC}}$	cartilage on femur and tibia
$\Omega := \Omega_{\text{Bo}} \cup \Omega_{\text{Ca}}$	bones and cartilages
$\Gamma_D := \Gamma_{\text{Fe,D}} \cup \Gamma_{\text{Ti,D}} \cup \Gamma_{\text{Fi,D}}$	Dirichlet boundaries of the bones
$\Gamma_N := \Gamma_{\text{Fe,N}} \cup \Gamma_{\text{Ti,N}} \cup \Gamma_{\text{Fi,N}}$	Neumann boundaries of the bones
$\Gamma_{\text{Fe,C}}, \Gamma_{\text{Ti,C}}$	contact boundaries of femur and tibia

Table 2.1. Notation for bones and cartilage

The femur and tibia domains are further supposed to be partitioned into two subdomains each, one for the bone proper, and one for the articular cartilage. The detailed notation for these domains is collected in Table 2.1.

We assume the domain boundaries to be piecewise once differentiable. Then an outward unit normal vector $\boldsymbol{\nu}$ exists almost everywhere. The femur and tibia boundaries consist of three disjoint parts each, on which we will prescribe contact, Dirichlet, or Neumann conditions. In particular, the contact boundaries of femur and tibia are those parts of the cartilage boundaries without intersection with the bone boundaries. The fibula boundary is only partitioned into Dirichlet and Neumann boundaries. In Section 2.3, additional patches for the ligament insertions will be introduced.

We want to describe the time evolution of a knee model in a time interval $[0, T]$. The deformation of the ensemble of bones and cartilage is denoted by a time-dependent displacement function $\mathbf{u} : \Omega \times [0, T] \to \mathbb{R}^3$. We assume the bones and cartilage to undergo small strains and small rotations only. Hence, strain can be measured by the linearized second-order strain tensor $\boldsymbol{\varepsilon}(\mathbf{u}) := \frac{1}{2}\left(\nabla \mathbf{u} + (\nabla \mathbf{u})^T\right)$. The corresponding stress tensor is denoted by $\boldsymbol{\sigma}$. We model the bones by a linear elastic material law

$$\boldsymbol{\sigma}_{\text{B}}(\mathbf{u}, x) := \mathbf{E}(x) : \boldsymbol{\varepsilon}(\mathbf{u}), \qquad x \in \Omega_{\text{Bo}},$$

and the cartilage layers by a linear viscoelastic Kelvin–Voigt law

$$\boldsymbol{\sigma}_{\text{V}}(\mathbf{u}, \dot{\mathbf{u}}, x) := \mathbf{E}(x) : \boldsymbol{\varepsilon}(\mathbf{u}) + \mathbf{V}(x) : \boldsymbol{\varepsilon}(\dot{\mathbf{u}}), \qquad x \in \Omega_{\text{Ca}},$$

where a superposed dot denotes the derivative with respect to time. The elasticity and viscosity tensors $\mathbf{E}$ and $\mathbf{V}$ may implement anisotropic and x-dependent behavior, as long as they are sufficiently smooth, bounded, uniformly positive definite in x, and show the usual symmetry properties. The ':'-symbol denotes the contraction of two tensors.

Using conservation of linear momentum we obtain the standard strong formulation of the equations of motion

$$\rho \ddot{\mathbf{u}} - \text{div}\, \boldsymbol{\sigma} = -\rho g \mathbf{z}, \qquad \text{in } \Omega, \quad t \in [0, T], \qquad (2.1)$$

where ρ is the material density, g is the gravitational acceleration, and $\mathbf{z}$ a unit vector pointing in the direction of negative gravity. To obtain a well-posed problem we need to prescribe initial conditions

$$\mathbf{u}(x,0) = \mathbf{u}_0(x) \quad \text{and} \quad \dot{\mathbf{u}}(x,0) = \dot{\mathbf{u}}_0(x) \quad \text{for all } x \in \Omega,$$

and boundary conditions

$$\mathbf{u}(x,t) = \mathbf{u}_D(x,t) \qquad x \in \Gamma_D,\ t \in [0,T] \qquad (2.2a)$$

$$\frac{\partial \mathbf{u}}{\partial \boldsymbol{\nu}}(x,t) = \mathbf{u}_N(x,t) \qquad x \in \Gamma_N,\ t \in [0,T]. \qquad (2.2b)$$

In our context, prescribed surface tractions $\mathbf{u}_N$ may model, e.g., the interaction of muscle forces with the joint.

Finally, we need to specify the relation between femur and tibia. We model this as a contact problem, i.e., femur and tibia are allowed to move freely with respect to each other, but they may not interpenetrate. Note that, since the relevant parts of femur and tibia are covered with cartilage layers, we are actually dealing with a contact problem for these layers.

For the mathematical modeling we exploit the simplifying assumption that strains are small. Additionally we assume that there is little tangential motion at the contact boundaries. This leads to the well-known Signorini conditions for contact problems [15,23]. On the contact boundaries $\Gamma_{\mathrm{Fe,C}}$ and $\Gamma_{\mathrm{Ti,C}}$ of femur and tibia cartilage, let there be a bijective and smooth mapping

$$\phi : \Gamma_{\mathrm{Fe,C}} \to \Gamma_{\mathrm{Ti,C}},$$

which identifies a priori the two contact boundaries with each other (Figure 2.2). We call ϕ a contact mapping. With respect to this contact mapping we define the reference gap function between the cartilage

$$g : \Gamma_{\mathrm{Fe,C}} \to \mathbb{R}, \quad g(x) := |x - \phi(x)|,$$

and the relative displacement in normal direction

$$[\mathbf{u}(x,t) \cdot \boldsymbol{\nu}]_\phi := \big(\mathbf{u}_{\mathrm{Fe}}(x,t) - \mathbf{u}_{\mathrm{Ti}}(\phi(x),t)\big) \cdot \boldsymbol{\nu}(x), \quad (2.3)$$

for $x \in \Gamma_{\mathrm{Fe,C}}$, $t \in [0,T]$. The linearized non-penetration condition is then

$$[\mathbf{u}(x,t) \cdot \boldsymbol{\nu}]_\phi \le g(x), \quad x \in \Gamma_{\mathrm{Fe,C}},\ t \in [0,T]. \qquad (2.4)$$

We now write the strong time-dependent contact problem in a variational form. For any open subset U of $\mathbb{R}^3$ let $L_2(U)$ be the space of square-integrable functions on U and we define $\mathbf{L}_2(U) := (L_2(U))^3$. The usual first order Sobolev space is denoted by $\mathbf{H}^1$. Its dual space is $(\mathbf{H}^1)^*$, and for the dual pairing the notation $\langle \cdot, \cdot \rangle_{\mathbf{H}^1}$ is used. We denote by $\mathbf{H}_D^1$ the set of $\mathbf{H}^1$-functions that satisfy the Dirichlet conditions in the sense of traces.

Let the bilinear form

$$a(\mathbf{v},\mathbf{w}) := \int_\Omega \varepsilon(\mathbf{v}) : \mathbf{E}(x) : \varepsilon(\mathbf{w})\,dx, \qquad \mathbf{v},\mathbf{w} \in \mathbf{H}^1(\Omega)$$

define the elastic energy of the bones and cartilage and

$$b(\mathbf{v},\mathbf{w}) := \int_{\Omega_{\mathrm{Ca}}} \varepsilon(\mathbf{v}) : \mathbf{V}(x) : \varepsilon(\mathbf{w})\,dx, \quad \mathbf{v},\mathbf{w} \in \mathbf{H}^1(\Omega_{\mathrm{Ca}})$$
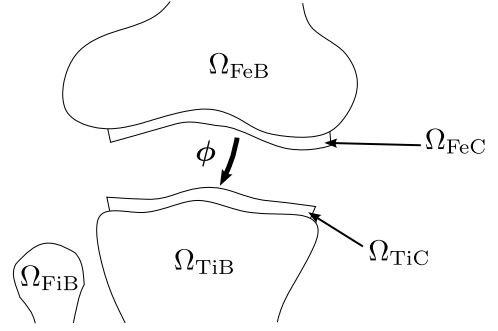$$(2.5)$$

Fig. 2.2. The geometry of the contact problem

the viscous contribution in the cartilage. Both bilinear forms are bounded in $\mathbf{H}^1$. We extend $b(\cdot,\cdot)$ to functions defined on Ω by integrating over all of Ω in (2.5) and setting $\mathbf{V}(x) = 0$ in $\Omega \setminus \Omega_{\mathrm{Ca}}$.

If $\mathbf{u}_N(\cdot,t) \in (\mathbf{H}^{1/2})^*(\Gamma_N)$ for almost every $t \in [0,T]$, the external forces are represented by the linear functional

$$f_{\mathrm{ext}}(\mathbf{v}) := -\int_\Omega \rho g \mathbf{z} \mathbf{v}\,dx + \langle \mathbf{u}_N, \mathbf{v} \rangle_{\mathbf{H}^{1/2}(\Gamma_N)}, \quad \mathbf{v} \in \mathbf{H}^1(\Omega),$$
$$(2.6)$$

where the dual pairing is to be understood in the sense of traces. The external forces consist of gravity in form of a volume force, and of Neumann data $\mathbf{u}_N$, which can be used, e.g., to model the soft tissue influence.

To the combined elastic and external forces we associate an operator $\mathbf{F} : \mathbf{H}^1(\Omega) \to (\mathbf{H}^1)^*(\Omega)$, defined by

$$\langle \mathbf{F}(\mathbf{w}), \mathbf{v} \rangle_{\mathbf{H}^1} := a(\mathbf{w},\mathbf{v}) - f_{\mathrm{ext}}(\mathbf{v}), \qquad \mathbf{v},\mathbf{w} \in \mathbf{H}^1(\Omega).$$

Likewise, we associate an operator $\mathbf{G} : \mathbf{H}^1(\Omega) \to (\mathbf{H}^1)^*(\Omega)$ to the viscoelastic forces by setting

$$\langle \mathbf{G}(\mathbf{w}), \mathbf{v} \rangle_{\mathbf{H}^1} := b(\mathbf{w},\mathbf{v}), \qquad \mathbf{v},\mathbf{w} \in \mathbf{H}^1(\Omega).$$

Both operators $\mathbf{F}$ and $\mathbf{G}$ are continuous.

The linearized nonpenetration condition (2.4) restricts the set of possible solutions. For a given gap function $g \in \mathbf{H}^{1/2}(\Gamma_{\mathrm{Fe,C}})$ we define the set of admissible displacements

$$\mathcal{K} := \big\{ \mathbf{v} \in \mathbf{H}_D^1(\Omega) \,\big|\, [\mathbf{v} \cdot \boldsymbol{\nu}]_\phi \le g \text{ a.e. on } \Gamma_{\mathrm{Fe,C}} \big\} \subset \mathbf{H}^1(\Omega).$$
$$(2.7)$$

The set $\mathcal{K}$ is closed and convex, and has the characteristic functional

$$I_\mathcal{K} : \mathbf{H}^1(\Omega) \to \mathbb{R} \cup \{\infty\}, \qquad I_\mathcal{K}(\mathbf{u}) = \begin{cases} 0 & \text{if } \mathbf{u} \in \mathcal{K} \\ \infty & \text{else}. \end{cases}$$

With this additional notation, the time-dependent contact problem (2.1), (2.2), (2.4) can be formulated as the variational inclusion

$$0 \in \rho\ddot{\mathbf{u}} + \mathbf{F}(\mathbf{u}) + \mathbf{G}(\dot{\mathbf{u}}) + \partial I_\mathcal{K}(\mathbf{u}), \qquad (2.8)$$

where $\partial I_\mathcal{K}$ is the subdifferential of $I_\mathcal{K}$ (see, e.g., [16]).

As shown, for instance, in [3], the unilateral contact problem between a viscoelastic body and a rigid foundation has at least one weak solution. However, uniqueness of solutions for general dynamical contact problems is still an open question.
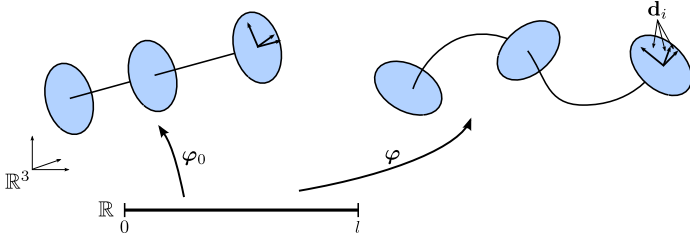
Fig. 2.3. Kinematics of a Cosserat rod

Remark 2.1. Note that we can intersect $\mathcal{K}$ with more sets of similar construction, to model further contact conditions or rigid couplings.

2.2 Ligaments as Cosserat Rods

Our model of the human knee contains four major ligaments, namely the anterior and posterior cruciate ligaments (ACL and PCL, resp.), and the lateral and medial collateral ligaments (LCL and MCL, resp.) (Figure 2.1). These are modeled by one-dimensional Cosserat materials (see, e.g., [50]), in order to reduce the model complexity and avoid meshing problems later on. This approach was first used in [43].

A Cosserat rod is a three-dimensional body that can be described by a continuous curve and a collection of two-dimensional planar cross-sections. Under load, the cross-sections remain unchanged in shape, but not necessarily normal to the deformed curve (Figure 2.3). Hence the motion of a rod in a time interval $[0,T]$ is described by a function

$$\varphi \; : \; [0,l] \times [0,T] \to \mathbb{R}^3 \times \mathrm{SO}(3)$$
$$\varphi(s,t) = (\mathbf{r}(s,t), R(s,t)),$$

where $\mathrm{SO}(3)$ is the special orthogonal group, i.e., the group of all matrices R with $R^T = R^{-1}$ and positive determinant. For a simpler notation we additionally introduce the space $\mathrm{SE}(3) := \mathbb{R}^3 \times \mathrm{SO}(3)$ of orientation-preserving rigid-body motions in $\mathbb{R}^3$ (the special Euclidean group). Elements of $\mathrm{SE}(3)$ will be written as $(\mathbf{r}, R)$.

We single out one static configuration $\varphi_0 : [0,l] \to \mathrm{SE}(3)$ and call it the reference configuration. For simplicity we assume that in the reference configuration φ_0 the centerline is parametrized by arc length. We do not assume that the reference configuration is identical to the rod configuration at time $t = 0$.

It is customary to interpret the columns of the matrix $R(s,t)$ as an orthogonal frame of unit vectors $\mathbf{d}_1$, $\mathbf{d}_2$, $\mathbf{d}_3$, of which the first two span the plane of the cross section. The orientation $R_0(s) = (\mathbf{d}_1^0|\mathbf{d}_2^0|\mathbf{d}_3^0)$ in the reference configuration is chosen such that $\mathbf{d}_1^0$ and $\mathbf{d}_2^0$ are directed along the principal axes of the cross-section.

We assume that the reference configuration φ_0 is provided with a positive mass density function $A_\rho(s) > 0$, which we interpret as the three-dimensional mass density integrated over the cross-sections. We also postulate the existence of a field of positive definite (uniformly in s)

3×3 rotatory inertia tensors $I_0(s)$ in the reference configuration. From this results a time-dependent rotatory inertia field

$$\mathbf{i}_\rho(s,t) = R(s,t)I_\rho(s)R^T(s,t)$$
$$= \sum_{\alpha,\beta=1}^{2} I_\rho^{\alpha\beta}(s)\mathbf{d}_\alpha \otimes \mathbf{d}_\beta + I_\rho^{33}(s)\mathbf{d}_3 \otimes \mathbf{d}_3$$

of the rod. The coefficients $I_\rho^{\alpha\beta}(s)$, $1 \leq \alpha,\beta \leq 2$ correspond to the moments of inertia of the cross-section located at s relative to the axes $\{\mathbf{d}_1^0, \mathbf{d}_2^0\}$ of the body frame. Similarly, the coefficient $I_\rho^{33}(s)$ is interpreted as the polar moment of inertia of the cross-section, relative to the body axis $\mathbf{d}_3^0$ [50].

The spatial velocity fields are given by

$$\mathbf{v} = \dot{\mathbf{r}} \qquad \text{and} \qquad \dot{R} = \hat{w}R = R\hat{W}.$$

Here, a superposed hat denotes the skew-symmetric matrix $\hat{w}$ associated to a vector $w \in \mathbb{R}^3$ by the relation $\hat{w}c = w \times c$ for all $c \in \mathbb{R}^3$. The vectors w and W are the spatial and body angular velocities, respectively. Together with the density function A_ρ and the inertia tensors we can express the linear and angular momenta as

$$\mathbf{p} = A_\rho\mathbf{v} \qquad \text{and} \qquad \boldsymbol{\pi} = \mathbf{i}_\rho w = RI_\rho W$$

via the Legendre transform.

A suitable strain measure for the rods is

$$(\boldsymbol{\Gamma}, \hat{\boldsymbol{\Omega}}) \in \mathbb{R}^3 \times \mathfrak{so}(3) \qquad (\boldsymbol{\Gamma}, \hat{\boldsymbol{\Omega}}) = (R^{-1}\mathbf{r}', R^{-1}R') - (R_0^{-1}\mathbf{r}_0', R_0^{-1}R_0')$$

where a prime denotes derivation with respect to s. It is easily verified that rigid body transformations leave $(\boldsymbol{\Gamma}, \hat{\boldsymbol{\Omega}})$ invariant. The components of $\boldsymbol{\Gamma}$ and $\boldsymbol{\Omega}$ can be interpreted physically. The components $\boldsymbol{\Gamma}_1$ and $\boldsymbol{\Gamma}_2$ are the shear strains, while $\boldsymbol{\Gamma}_3$ is the stretching strain. The components $\boldsymbol{\Omega}_1$ and $\boldsymbol{\Omega}_2$ are the bending strains, and $\boldsymbol{\Omega}_3$ the strain related to torsion.

The stress quantities dual to $\boldsymbol{\Gamma}$ and $\boldsymbol{\Omega}$ are the total forces $\mathbf{n} : [0,l] \to \mathbb{R}^3$ and total moments (about $\mathbf{r}$) $\mathbf{m} : [0,l] \to \mathbb{R}^3$ across each cross section. The strong equations of motion of a dynamic Cosserat rod in a constant gravitational field can then be derived from the balance laws of linear and angular momentum (see [50])

$$\begin{aligned} \mathbf{n}' - A_\rho g\mathbf{z} &= \dot{\mathbf{p}} \\ \mathbf{m}' + \mathbf{r}' \times \mathbf{n} &= \dot{\boldsymbol{\pi}}. \end{aligned} \qquad (2.9)$$

Here, $\mathbf{z}$ is again the unit vector in the direction of negative gravity. The equations can be supplemented with the usual Dirichlet- and Neumann-type boundary conditions. However, in our knee model the rod boundaries are not true boundaries but instead couple with the bones. We discuss suitable coupling conditions in the next section.

As in standard continuum mechanics a material law links the internal forces and moments to the strains. A Cosserat rod is called hyperelastic if there exists an energy functional $W(\boldsymbol{\Gamma}, \boldsymbol{\Omega})$ such that

$$\mathbf{n} = \frac{\partial W}{\partial \boldsymbol{\Gamma}}(\boldsymbol{\Gamma}, \boldsymbol{\Omega}), \qquad \mathbf{m} = \frac{\partial W}{\partial \boldsymbol{\Omega}}(\boldsymbol{\Gamma}, \boldsymbol{\Omega}).$$

We use a diagonal linear elastic material, where

$$W(w, z) = \frac{1}{2} \begin{pmatrix} w \\ z \end{pmatrix}^T \mathbf{W} \begin{pmatrix} w \\ z \end{pmatrix}, \qquad (2.10)$$
$$\mathbf{W} := \mathrm{diag}(A_1, A_2, A_3, K_1, K_2, K_3),$$

with positive parameters A_i, K_i, $i = 1, 2, 3$. These parameters can be interpreted as follows [22]. Let $|\mathcal{A}(s)|$ be the surface area of the cross-section at s. Then

$$A_1 = A_2 = \frac{E}{(2 + 2\nu)}|\mathcal{A}|, \quad A_3 = E|\mathcal{A}|$$

with Young's modulus E and the Poisson ratio $\nu \in (0, \frac{1}{2})$. Further,

$$K_1 = EJ_1, \quad K_2 = EJ_2, \quad K_3 = \frac{E}{(2 + 2\nu)}J_3,$$

where J_1 and J_2 are the second moments of area of the cross-section and $J_3 = J_1 + J_2$ is the polar moment of inertia. These moments describe how the shape of the cross-section influences the deformation behavior of the rod.

The equilibrium equations (2.9) have a weak formulation. Let $Q := H^1([0, l], \mathbb{R}^3 \times \mathrm{SO}(3))$ denote the (nonlinear) set of rod configurations. We introduce the linear space Y of test functions

$$Y := H^1([0, l], \mathbb{R}^3 \times \mathfrak{so}(3)).$$

Admissible variations to a configuration $\boldsymbol{\varphi} = (\mathbf{r}, R) \in Q$ span the tangent space $T_{\boldsymbol{\varphi}}Q$ in the sense that

$$T_{\boldsymbol{\varphi}}Q := \{(\mathbf{r} + u, \hat{\theta}R) : (u, \theta) \in Y\}.$$

Formally, the dynamic weak formulation of the momentum equations is constructed by taking the dot product of (2.9) with a test function in Y, integrating over $[0, l]$ and using the divergence theorem [50]. The result is

$$\int_0^l [\dot{\boldsymbol{\pi}} \cdot \boldsymbol{\mu} + \dot{\mathbf{p}} \cdot \boldsymbol{\eta}]\, ds + \int_0^l [\mathbf{n} \cdot (\boldsymbol{\eta}' - \boldsymbol{\mu} \times \mathbf{r}') + \mathbf{m} \cdot \boldsymbol{\mu}']\, ds$$
$$= -\int_0^l A_\rho g \mathbf{z} \boldsymbol{\eta}\, ds$$

$$(2.11)$$

for any test function $(\boldsymbol{\eta}, \hat{\boldsymbol{\mu}}) \in Y$.

2.3 Coupled Bone–Ligament System

In the previous section we have hardly mentioned the boundary conditions for the rod problems. In our model, they appear in the form of coupling conditions that connect the rods to the bone models. The coupling conditions result from a heuristic dimensional reduction of the corresponding conditions for two three-dimensional object [43,47]. A more rigorous analysis is given in [44].

In the following, let L stand for any one of the four ligaments in our knee model, L $\in \{\mathrm{ACL, PCL, MCL, LCL}\}$.
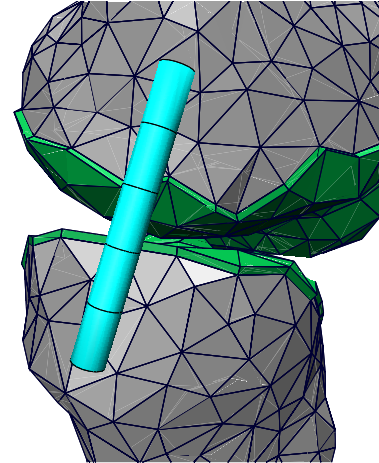

Fig. 2.4. The model of the medial collateral ligament (MCL) and the femur and tibia bones in the initial configuration. Shown is a discretization with fairly coarse finite element grids.

The corresponding Cosserat rod is described by a configuration function

$$\boldsymbol{\varphi}_{\mathrm{L}} \; : \; [0, l_{\mathrm{L}}] \times [0, T] \to \mathrm{SE}(3).$$

Each ligament connects two bones. In particular, the ACL, PCL, and MCL connect the femur to the tibia, and the LCL connects the femur to the fibula. Therefore, on the femur we mark four (relatively) open disjoint subsets of the boundary, and call them $\Gamma_{\mathrm{Fe,L}}$, with L $\in \{\mathrm{ACL, PCL, MCL, LCL}\}$. Similarly, we mark three coupling patches on the tibia boundary and one on the fibula boundary. These patches are not expected to be flat, even though they will be coupled to the Cosserat rods, whose ends are modeled by flat cross-sections.

For each of the four rods $\boldsymbol{\varphi}_{\mathrm{L}}$ let the left boundary $\{0\}$ of its parameter domain $[0, l_{\mathrm{L}}]$ be the proximal end, and the right boundary $\{l_{\mathrm{L}}\}$ the distal end. If $\boldsymbol{\varphi}_{\mathrm{L}}$ connects bone A to bone B we set the initial configuration $\boldsymbol{\varphi}_{\mathrm{L}}(\cdot, 0) = (\mathbf{r}_{\mathrm{L}}(\cdot, 0), R_{\mathrm{L}}(\cdot, 0))$ as

$$\mathbf{r}_{\mathrm{L}}(s, 0) = \frac{1-s}{|\Gamma_{A,\mathrm{L}}|}\int_{\Gamma_{A,\mathrm{L}}} x\, dx + \frac{s}{|\Gamma_{B,\mathrm{L}}|}\int_{\Gamma_{B,\mathrm{L}}} x\, dx$$

(with $|\Gamma_{A,\mathrm{L}}|$, $|\Gamma_{B,\mathrm{L}}|$ the areas of the patches $\Gamma_{A,\mathrm{L}}$, $\Gamma_{B,\mathrm{L}}$, resp.), and $R_{\mathrm{L}}(s, 0)$ constant and such that $\mathbf{d}_3(s, 0)$ is parallel to the line segment traced out by $\mathbf{r}_{\mathrm{L}}(\cdot, 0)$. This is illustrated in Figure 2.4. For each rod we set a reference configuration

$$\boldsymbol{\varphi}_{0,\mathrm{L}} = (\mathbf{r}_{0,\mathrm{L}}, R_{0,\mathrm{L}}), \quad \mathbf{r}_{0,\mathrm{L}}(s) = (0, 0, s)^T, \quad R_{0,\mathrm{L}}(s) = \mathrm{Id}.$$

This is the state where the rod is stress-free. It cannot be realized anatomically, i.e., without detaching the ligament from the bone. In general, the ligament length in the stress-free reference configuration is shorter than in the initial configuration

$$l_{\mathrm{L}} < \left| \frac{1}{|\Gamma_{A,\mathrm{L}}|}\int_{\Gamma_{A,\mathrm{L}}} x\, dx - \frac{1}{|\Gamma_{B,\mathrm{L}}|}\int_{\Gamma_{B,\mathrm{L}}} x\, dx \right|.$$

This length difference is the so-called pre-strain, which is a model parameter. It leads to a constant tensile stress in the direction of $\mathbf{d}_3$ in the rods at $t = 0$.

It is known from general domain decomposition theory that a coupling problem for two second-order equations requires coupling conditions for the primal and the dual variables [42]. In our case the primal variables are the displacements $\mathbf{u}$ of the continua, and the position $\mathbf{r}$ and orientation R of the rod cross-sections. The dual variables are the stresses $\boldsymbol{\sigma}$ in the continua and force and torque vectors $\mathbf{n}, \mathbf{m}$ of the rods.

We begin with the conditions for the primal variables. Let Γ be one of the ligament insertion patches, $\mathbf{u}$ the deformation function of the corresponding bone, and $\boldsymbol{\varphi}$ the configuration of the rod attached at Γ. Without loss of generality we assume that $\boldsymbol{\varphi}$ attaches to Γ at the proximal end, i.e., at $s = 0$. We first require that the position of the center line be the average position of the deformed coupling boundary Γ for all $t \in [0, T]$

$$\mathbf{r}(0, t) = \frac{1}{|\Gamma|} \int_{\Gamma} (\mathbf{u}(x, t) + x) \, dx. \qquad (2.12)$$

To derive a coupling condition for the cross-section orientations we first define the average deformation of the interface Γ at time t

$$\mathcal{F}(\mathbf{u}, t) := \frac{1}{|\Gamma|} \int_{\Gamma} \nabla(\mathbf{u}(x, t) + x) \, dx.$$

In the regime of linear elasticity this is a regular matrix. We can use the polar decomposition to split the average deformation into a rotation and a stretching part

$$\mathcal{F}(\mathbf{u}, t) = \mathrm{polar}(\mathcal{F}(\mathbf{u}, t)) H(\mathbf{u}, t),$$

and we call the orthogonal matrix $\mathrm{polar}(\mathcal{F}(\mathbf{u}, t))$ the average orientation of the interface under $\mathbf{u}$. If the bones are in the initial configuration, i.e., $\mathbf{u} \equiv 0$, then $\mathrm{polar}(\mathcal{F}(\mathbf{u}))$ equals the identity Id. At the same time, the orientation of the corresponding rod cross section is $R(0, 0)$. Having a rigid junction means that this relative orientation is preserved for all times. Hence we postulate the orientation coupling conditions

$$\mathrm{polar}(\mathcal{F}(\mathbf{u}, t)) R(0, 0) = R(0, t) \qquad (2.13)$$

for all $t \in [0, T]$.

To get a well-defined system of equations we also need to find coupling conditions for the dual variables $\boldsymbol{\sigma}, \mathbf{n}, \mathbf{m}$. These can be derived by requiring that the total force and moment transmitted across the interface be preserved. We obtain

$$\int_{\Gamma} \boldsymbol{\sigma}(\mathbf{u}) \nu \, ds = -\mathbf{n}(0) \nu_0$$
$$\int_{\Gamma} (x - \mathbf{r}(0)) \times (\boldsymbol{\sigma}(\mathbf{u}) \nu) \, ds = -\mathbf{m}(0) \nu_0, \qquad (2.14)$$

where ν denotes the unit outer normal of the interface Γ, and $\nu_0 = -1$ is the unit outer normal of the rod parameter domain $[0, l_L]$ at $s = 0$ [43, 47].

3 Time Discretizations

In this section, we describe the time discretization for the dynamic coupled problem. As the two submodels show very different features we use different time integrators for each of them. The result is a sequence of coupled continuous problems. Hence we are in the framework of the method of time layers, also known as Rothe's method [13]. The discretization in space will be dealt with in Chapter 4.

3.1 Contact-Stabilized Newmark Method for Bones and Cartilage

When constructing a time-stepping method for the dynamic contact problem (2.8), the challenges are to maintain energy conservation or at least dissipativity, and to avoid numerical artifacts such as the flutter observed in [12,24]. We achieve both by a Newmark method enhanced with a contact-stabilization step.

Let the time interval $[0, T]$ be subdivided by $N_\triangle + 1$ discrete time points $0 = t_0 < t_1 < \cdots < t_{N_\triangle} = T$. We call τ the time step size, and assume that it is constant purely for simplicity of notation.[2]

Let $n \in \mathbb{N}$ be the iteration number. The discrete quantities $\mathbf{u}^n$ and $\dot{\mathbf{u}}^n$ are assumed to be algorithmic approximations of the displacement $\mathbf{u}(t_n)$ and the velocity $\dot{\mathbf{u}}(t_n)$, respectively. The underlying concept of the contact-stabilized Newmark discretization are Taylor expansions of displacements and velocities, and a fully implicit treatment of the contact forces. Algorithmically, we obtain a predictor–corrector-type method where a single predictor step for the displacements $\mathbf{u}_{\mathrm{pred}}^{n+1}$ is followed by corrector steps for the displacements $\mathbf{u}^{n+1}$ and velocities $\dot{\mathbf{u}}^{n+1}$:

$$0 \in \mathbf{u}_{\mathrm{pred}}^{n+1} - \left(\mathbf{u}^n + \tau \dot{\mathbf{u}}^n\right) + \partial I_{\mathcal{K}}\left(\mathbf{u}_{\mathrm{pred}}^{n+1}\right) \qquad (3.1a)$$

$$0 \in \mathbf{u}^{n+1} - \mathbf{u}_{\mathrm{pred}}^{n+1} + \frac{\tau^2}{2}\left(\mathbf{F}\left(\frac{\mathbf{u}^n + \mathbf{u}^{n+1}}{2}\right)\right.$$
$$\left. + \mathbf{G}\left(\frac{\mathbf{u}^{n+1} - \mathbf{u}^n}{\tau}\right) + \partial I_{\mathcal{K}}\left(\mathbf{u}^{n+1}\right)\right) \qquad (3.1b)$$

$$\dot{\mathbf{u}}^{n+1} = \frac{\mathbf{u}_{\mathrm{pred}}^{n+1} - \mathbf{u}^n}{\tau} - \tau\left(\mathbf{F}\left(\frac{\mathbf{u}^n + \mathbf{u}^{n+1}}{2}\right)\right.$$
$$\left. + \mathbf{G}\left(\frac{\mathbf{u}^{n+1} - \mathbf{u}^n}{\tau}\right) - \mathbf{F}_{\mathrm{con}}\left(\mathbf{u}^{n+1}\right)\right).$$

The contact forces $\mathbf{F}_{\mathrm{con}}(\mathbf{u}^{n+1})$ are defined by

$$\frac{\tau^2}{2}\left\langle \mathbf{F}_{\mathrm{con}}(\mathbf{u}^{n+1}), \mathbf{v}\right\rangle_{\mathbf{H}^1} := \left\langle \mathbf{u}^{n+1} - \mathbf{u}_{\mathrm{pred}}^{n+1} + \frac{\tau^2}{2}\left[\mathbf{F}\left(\frac{\mathbf{u}^n + \mathbf{u}^{n+1}}{2}\right)\right.\right.$$
$$\left.\left. + \mathbf{G}\left(\frac{\mathbf{u}^{n+1} - \mathbf{u}^n}{\tau}\right)\right], \mathbf{v}\right\rangle_{\mathbf{H}^1}, \qquad \mathbf{v} \in \mathbf{H}^1.$$

In each time step, the method requires the solution of the nonlinear variational inclusion (3.1b), which is equivalent to a constrained, quadratic, convex minimization problem.

---

[2] An adaptive time step control for the contact-stabilized Newmark method has been presented in [27,24].

Theorem 3.1. *The variational inclusion* (3.1b) *is equivalent to the minimization problem*

$$\mathbf{u}^{n+1} = \arg\min_{\mathbf{v}\in\mathcal{K}} \left[\frac{1}{2}g(\mathbf{v},\mathbf{v}) - \tau^2 f_{\text{ext}}(\mathbf{u}^n + \mathbf{v})\right] \quad (3.2)$$

where

$$g(\mathbf{v},\mathbf{v}) = \left\|\mathbf{v} - \mathbf{u}_{\text{pred}}^{n+1}\right\|_{\mathbf{L}_2}^2 + \tau^2 a\left(\frac{\mathbf{u}^n+\mathbf{v}}{2}, \frac{\mathbf{u}^n+\mathbf{v}}{2}\right) \\ + \frac{\tau}{2}b\left(\frac{\mathbf{v}-\mathbf{u}^n}{\tau}, \frac{\mathbf{v}-\mathbf{u}^n}{\tau}\right), \quad (3.3)$$

and $\mathcal{K}$ *is given by* (2.7).

The proof is based on the theory of [16, Chap. 5]. The constrained minimization problem (3.2) has the same structure as a static contact problem in linear elasticity [57,58]. Its solution is the most expensive part of the Newmark scheme.

The term $\partial I_\mathcal{K}(\mathbf{u}_{\text{pred}}^{n+1})$ in the predictor step (3.1a) is the aforementioned contact stabilization. It turns out that the variational inclusion (3.1a) can equivalently be written as the convex minimization problem

$$\mathbf{u}_{\text{pred}}^{n+1} = \arg\min_{\mathbf{v}\in\mathcal{K}} \frac{1}{2}\left\|\mathbf{v} - (\mathbf{u}^n + \tau\dot{\mathbf{u}}^n)\right\|_{\mathbf{L}_2}^2. \quad (3.4)$$

As $\mathcal{K}$ only restricts values on the contact boundary, $\mathbf{u}^n + \tau\dot{\mathbf{u}}^n$ and its $\mathbf{L}_2$-projection onto $\mathcal{K}$ only differ on a set of measure zero. Hence, in a Lebesgue-space setting, the projection (3.4) is void. However, the same projection in a finite element space will be the key factor in avoiding numerical oscillations [12,24].

Compared to classical Newmark schemes for contact problems, the contact-stabilized variant has various advantages concerning momentum conservation and energy behavior. First of all, the linear momentum of the system is preserved by the discretized system.

Theorem 3.2 (Linear momentum conservation [24]). *The contact-stabilized Newmark method conserves the linear momentum if* $f_{\text{ext}} = 0$ *and* $\Gamma_D = \emptyset$.

Conservation of the angular momentum cannot be expected, because, due to the linearized contact conditions, not even the continuous contact problem (2.8) conserves the angular momentum [24,34].

The implicit handling of the non-penetration constraints leads to energy dissipativity of the discrete evolution in the presence of contact. In the absence of contact, the algorithm is even energy conserving, if the viscous energy is taken into account.

Theorem 3.3 (Energy dissipativity [24]). *Assume that* $f_{\text{ext}} = 0$. *If* $\mathbf{u}_{\text{pred}}^{n+1}$ *and* $\mathbf{u}^{n+1}$ *are not in contact, i.e., if* $[\mathbf{u}_{\text{pred}}^{n+1}\cdot\boldsymbol{\nu}]_\phi < g$ *and* $[\mathbf{u}^{n+1}\cdot\boldsymbol{\nu}]_\phi < g$ *a.e. on* $\Gamma_{Fe,C}$, *then the contact-stabilized Newmark method is energy conserving (including the viscous energy). If* $\mathbf{u}_{\text{pred}}^{n+1}$ *and* $\mathbf{u}^{n+1}$ *are only in contact where* $\mathbf{u}^n$ *has already been in contact, i.e., if* $[\mathbf{u}_{\text{pred}}^{n+1}\cdot\boldsymbol{\nu}]_\phi = [\mathbf{u}^{n+1}\cdot\boldsymbol{\nu}]_\phi = g$ *a.e. on* $\widetilde{\Gamma} \subset \Gamma_{Fe,C}$ *where* $[\mathbf{u}^n\cdot\boldsymbol{\nu}]_\phi = g$ *a.e., then the algorithm is also energy conserving. Otherwise, the algorithm is energy dissipative.*

In the unconstrained case, the Newmark scheme is well-known to be second-order consistent (see, e.g., [19]). In the case of contact constraints, however, the question of consistency requires a novel regularity assumption on the solution and its derivatives because of the discontinuities at contact interfaces. For a function tuple $(\mathbf{v},\dot{\mathbf{v}}) : [t, t+\tau] \to \mathbf{H}^1\times\mathbf{L}_2$ with $\dot{\mathbf{v}} \in \mathbf{L}_2((t, t+\tau), \mathbf{H}^1)$, define the physical energy norm [25]

$$\|(\mathbf{v},\dot{\mathbf{v}})\|_{\mathcal{E}(t,\tau)}^2 := \frac{1}{2}\|\dot{\mathbf{v}}(t+\tau)\|_{\mathbf{L}_2}^2 + \frac{1}{2}a(\mathbf{v}(t+\tau), \mathbf{v}(t+\tau)) \\ + \int_t^{t+\tau} b(\dot{\mathbf{v}}(s), \dot{\mathbf{v}}(s))\,ds.$$

It may be interpreted as the sum of the kinetic energy, the potential energy, and a viscoelastic part. In the following theorem, the continuous evolution operator $\bar{\boldsymbol{\Phi}} = (\boldsymbol{\Phi}, \dot{\boldsymbol{\Phi}})$ represents the state of a continuous solution $(\mathbf{u}, \dot{\mathbf{u}})$ and $\bar{\boldsymbol{\Psi}} = (\boldsymbol{\Psi}, \dot{\boldsymbol{\Psi}})$ denotes the discrete evolution operator. $\text{TV}(\mathbf{v}, [t_0, T], \mathbf{V})$ is the variation of a function $\mathbf{v} : [t_0, T] \to \mathbf{V}$, and $\text{BV}([t_0, T], \mathbf{V})$ means the set of all functions from $[t_0, T]$ into $\mathbf{V}$ that have bounded variation [48].

Theorem 3.4 (Consistency error [24]).
Let $\dot{\mathbf{u}} \in \text{BV}([t, t+\tau], \mathbf{H}^1)$ *and* $\ddot{\mathbf{u}} \in \text{BV}([t, t+\tau], (\mathbf{H}^1)^*)$. *Then, for initial values* $\mathbf{u}^n = \mathbf{u}(t)$ *and* $\dot{\mathbf{u}}^n = \dot{\mathbf{u}}(t)$, *the consistency error of the contact-stabilized Newmark method satisfies*

$$\left\|\bar{\boldsymbol{\Psi}} - \bar{\boldsymbol{\Phi}}\right\|_{\mathcal{E}(t,\tau)} = R(\mathbf{u}, [t, t+\tau]) \cdot O(\tau^{1/2}),$$

where

$$R(\mathbf{u}, [t, t+\tau]) := \text{TV}(\mathbf{u}, [t, t+\tau], \mathbf{H}^1) + \text{TV}(\dot{\mathbf{u}}, [t, t+\tau], \mathbf{H}^1) \\ + \text{TV}(\ddot{\mathbf{u}}, [t, t+\tau], (\mathbf{H}^1)^*).$$

A detailed analysis of the contact-stabilized Newmark method can be found in [12,26,24].

3.2 Energy–Momentum Method for Cosserat Rods

For the time-dependent Cosserat rod problems, the main difficulty is the nonlinearity of the configuration space Q. We use the Energy–Momentum Method originally introduced by Simo and Tarnow for nonlinear elastodynamics [49], and applied to Cosserat rods in [50]. In this section we review only the actual time discretization. Our space discretization, which is quite different from the one used in [50], is presented in Chapter 4.3.

Let again the time interval $[0, T]$ be subdivided by the points $0 = t_0 < t_1 < \cdots < t_{N_\triangle} = T$ and let τ denote the time step size, for simplicity assumed to be constant. Let $\boldsymbol{\varphi}^n = (\mathbf{r}^n, R^n)$ and $\boldsymbol{\varphi}^{n+1} = (\mathbf{r}^{n+1}, R^{n+1})$ denote the configurations of the rod at times t_n and t_{n+1}, respectively.

To discretize the weak time-dependent rod problem (2.11) we first replace $\mathbf{r}$ by its average over two time steps $\mathbf{r}_{n+1/2} := \frac{1}{2}(\mathbf{r}^{n+1} + \mathbf{r}^n)$, and the stresses $\mathbf{n}$ and $\mathbf{m}$ by

suitable algorithmic approximations $\tilde{\mathbf{n}}$ and $\tilde{\mathbf{m}}$, respectively, to be specified later. Plugging these into (2.11), and replacing the time derivatives by forward differences, we obtain the following semi-discrete weak problem

$$
\frac{1}{\tau} \int_0^l (\boldsymbol{\pi}^{n+1} - \boldsymbol{\pi}^n) \cdot \boldsymbol{\mu} + (\mathbf{p}^{n+1} - \mathbf{p}^n) \cdot \boldsymbol{\eta} \, ds
$$
$$
+ \int_0^l \tilde{\mathbf{n}} \cdot (\boldsymbol{\eta}' - \boldsymbol{\mu} \times \mathbf{r}'_{n+1/2}) + \tilde{\mathbf{m}} \cdot \boldsymbol{\mu}' \, ds = - \int_0^l A_\rho g \mathbf{z} \boldsymbol{\eta} \, ds,
$$
$$(3.5)$$

which must hold for all test functions $(\boldsymbol{\eta}, \hat{\boldsymbol{\mu}}) \in Y$.

This system is now reformulated as an equation for two update variables $\boldsymbol{\delta} : [0, l] \to \mathbb{R}^3$ and $\boldsymbol{\theta} : [0, l] \to \mathfrak{so}(3)$ for the positions and orientations, respectively. The dependencies of $\boldsymbol{\delta}$ and $\boldsymbol{\theta}$ on the iteration number n is omitted for simplicity of notation. We introduce the Cayley transform $\mathrm{cay} : \mathfrak{so}(3) \to \mathrm{SO}(3)$ given by

$$
\mathrm{cay}\, \hat{\boldsymbol{\theta}} = \mathrm{Id} + \frac{1}{1 + \frac{1}{4}\|\boldsymbol{\theta}\|^2} \left[\hat{\boldsymbol{\theta}} + \frac{1}{2}\hat{\boldsymbol{\theta}}^2 \right],
$$

and note for later use that its inverse is given by

$$
\mathrm{cay}^{-1} R = 2(R + \mathrm{Id})^{-1}(R - \mathrm{Id}). \qquad (3.6)
$$

We then define the increments as

$$
\boldsymbol{\delta} := \frac{\tau}{2}(\mathbf{v}^{n+1} + \mathbf{v}^n) \qquad \text{and} \qquad \boldsymbol{\theta} := \frac{\tau}{2}(w^{n+1} + \mathrm{cay}[\boldsymbol{\theta}]w^n).
$$
$$(3.7)$$

The implicit definition of the rotation update $\boldsymbol{\theta}$ results from the midpoint approximation of the body angular velocities $\boldsymbol{\theta} = R^n \boldsymbol{\Theta} = R^n \frac{\tau}{2}(W^{n+1} - W^n)$. Given increments $\boldsymbol{\delta}$ and $\boldsymbol{\theta}$ and a configuration at time step n, a new configuration at time step $n+1$ can be computed by

$$
\mathbf{r}^{n+1} = \mathbf{r}^n + \boldsymbol{\delta} \qquad \text{and} \qquad R^{n+1} = \mathrm{cay}[\boldsymbol{\theta}]R^n. \quad (3.8)
$$

This time discretization scheme conserves the linear and angular momenta if the external forces vanish [50, Prop. 3.1]. Energy is conserved exactly if the algorithmic stresses $\tilde{\mathbf{n}}$ and $\tilde{\mathbf{m}}$ are chosen properly. For the following theorem denote by $\mathbf{W}_\Gamma$ and $\mathbf{W}_\Omega$ the upper and lower 3×3 diagonal blocks of the rod material matrix $\mathbf{W}$ defined in (2.10).

Theorem 3.5 (Energy conservation [50]). *Let the material law be linear elastic in the sense that there are matrices $\mathbf{W}_\Gamma$ and $\mathbf{W}_\Omega$ such that $\mathbf{N} = \mathbf{W}_\Gamma \boldsymbol{\Gamma}$ and $\mathbf{M} = \mathbf{W}_\Omega \boldsymbol{\Omega}$, and let the external loading be independent of $\boldsymbol{\varphi}$. Then the algorithmic system (3.5) and (3.7) conserves the energy if the algorithmic spatial stresses are given by*

$$
\tilde{\mathbf{N}} = \frac{1}{2}\mathbf{W}_\Gamma(\boldsymbol{\Gamma}^{n+1} + \boldsymbol{\Gamma}^n), \qquad \tilde{\mathbf{M}} = \frac{1}{2}\mathbf{W}_\Omega(\boldsymbol{\Omega}^{n+1} + \boldsymbol{\Omega}^n),
$$

and the algorithmic body stresses are linked to the spatial ones by

$$
\tilde{\mathbf{n}} = R_{n+1/2}\tilde{\mathbf{N}}, \qquad \tilde{\mathbf{m}} = \det[R_{n+1/2}]R_{n+1/2}^{-T}\tilde{\mathbf{M}},
$$
$$
R_{n+1/2} := \frac{1}{2}\left(R^{n+1} + R^n\right).
$$

A construction for nonlinear material laws can be found in [50].

To make the method applicable, we will now reformulate the semi-discrete system (3.5) in terms of the displacement and rotation increments $(\boldsymbol{\delta}, \hat{\boldsymbol{\theta}}) \in Y$. Introduce the helper function

$$
H(\boldsymbol{\theta}) := \frac{1}{1 + \frac{1}{4}\|\boldsymbol{\theta}\|^2}\left(\mathrm{Id} + \frac{1}{2}\hat{\boldsymbol{\theta}}\right)
$$

and note the relations (see [50])

$$
\det[R_{n+1/2}]R_{n+1/2}^{-T} = H(\boldsymbol{\theta})R^n, \qquad \boldsymbol{\Omega}_{n+1} - \boldsymbol{\Omega}_n = R_n^T H(\boldsymbol{\theta})^T \boldsymbol{\theta}'.
$$

Then, the dynamic part of (3.5) can be reformulated as

$$
\frac{1}{\tau} \int_0^l (\boldsymbol{\pi}^{n+1} - \boldsymbol{\pi}^n) \cdot \boldsymbol{\mu} + (\mathbf{p}^{n+1} - \mathbf{p}^n) \cdot \boldsymbol{\eta} \, ds
$$
$$
= \frac{1}{\tau} \int_0^l \left(\mathrm{cay}[\boldsymbol{\theta}]\mathbf{i}_\rho^n \, \mathrm{cay}[\boldsymbol{\theta}]^T \left(\frac{2}{\tau}\boldsymbol{\theta} - \mathrm{cay}[\boldsymbol{\theta}]w^n \right) - \mathbf{i}_\rho^n w^n \right) \cdot \boldsymbol{\mu} \, ds
$$
$$
+ \frac{1}{\tau} \int_0^l A_\rho \left(\frac{2}{\tau}\boldsymbol{\delta} - 2\mathbf{v}^n \right) \cdot \boldsymbol{\eta} \, ds
$$
$$
=: \mathrm{dyn}_{\boldsymbol{\varphi}^n}[(\boldsymbol{\delta}, \boldsymbol{\theta}); (\boldsymbol{\eta}, \boldsymbol{\mu})]. \qquad (3.9)
$$

Similarly, the potential part can be rewritten as

$$
\int_0^l \tilde{\mathbf{n}} \cdot (\boldsymbol{\eta}' - \boldsymbol{\mu} \times \mathbf{r}'_{n+1/2}) + \tilde{\mathbf{m}} \cdot \boldsymbol{\mu}' \, ds
$$
$$
= \int_0^l \frac{1}{4}(\mathrm{cay}[\boldsymbol{\theta}]R^n + R^n)\mathbf{W}_\Gamma
$$
$$
\cdot \left[R_n^T \mathrm{cay}[\boldsymbol{\theta}]^T(\boldsymbol{\delta}' + \mathbf{r}'_n) - R_0^T \mathbf{r}'_0 + \boldsymbol{\Gamma}^n \right] \cdot \left(\boldsymbol{\eta}' - \boldsymbol{\mu} \times \frac{1}{2}(\boldsymbol{\delta}' + 2\mathbf{r}'_n) \right) ds
$$
$$
+ \int_0^l H(\boldsymbol{\theta})R^n \frac{1}{2}\mathbf{W}_\Omega \left[R_n^T H(\boldsymbol{\theta})^T \boldsymbol{\theta}' + 2\boldsymbol{\Omega}^n \right] \cdot \boldsymbol{\mu}' \, ds
$$
$$
=: \mathrm{pot}_{\boldsymbol{\varphi}^n}[(\boldsymbol{\delta}, \boldsymbol{\theta}); (\boldsymbol{\eta}, \boldsymbol{\mu})]. \qquad (3.10)
$$

For each configuration $\boldsymbol{\varphi}^n : [0, l] \to \mathbb{R}^3 \times \mathrm{SO}(3)$, the forms $\mathrm{dyn}_{\boldsymbol{\varphi}^n}[\,\cdot\,;\,\cdot\,]$ and $\mathrm{pot}_{\boldsymbol{\varphi}^n}[\,\cdot\,;\,\cdot\,]$ are nonlinear in their first arguments, and linear in the second ones. The resulting system

$$
\frac{1}{\tau}\mathrm{dyn}_{\boldsymbol{\varphi}^n}[(\boldsymbol{\delta}, \boldsymbol{\theta}); (\boldsymbol{\eta}, \boldsymbol{\mu})] + \mathrm{pot}_{\boldsymbol{\varphi}^n}[(\boldsymbol{\delta}, \boldsymbol{\theta}); (\boldsymbol{\eta}, \boldsymbol{\mu})] =
$$
$$
- \int_0^l A_\rho g \mathbf{z} \boldsymbol{\eta} \, ds \qquad \forall(\boldsymbol{\eta}, \hat{\boldsymbol{\mu}}) \in Y
$$
$$(3.11)$$

is a nonlinear equation for the variables $(\boldsymbol{\delta}, \hat{\boldsymbol{\theta}})$ in the linear space Y, given in a weak formulation. Implementation of the energy–momentum method for Cosserat rods means solving (3.11) for each time step n, and using the update formulas (3.8) to obtain the configuration at the next time step.

4 Finite Element Discretizations

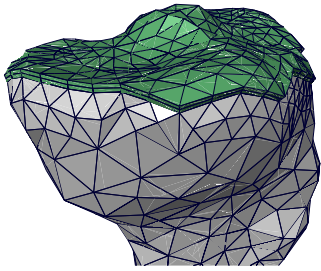The next step are the spatial discretizations of the different submodels. We will start with finite elements on

Fig. 4.1. Combined simplex–prism grid for the tibia and its articular cartilage, after one step of refinement

Fig. 4.2. Improving the quality of the cartilage grid after refinement with a boundary parametrization. Left: coarse prism grid with parametrizations (dashed lines) at the outer boundary and at the bone–cartilage interface. Center: refining the cartilage grid and using the parametrization to place the new boundary vertices produces a low-quality grid. Right: placing the interior vertices at uniform distances along their respective "columns" repairs the grid.

mixed simplex–prism grids for the bones and cartilage, and then describe a mortar technique for the discretization of the contact constraints. Geodesic finite elements will be used for the discretization of the Cosserat rod equations.

4.1 Discretization of Bones and Cartilage

The two domains Ω_{Fe} and Ω_{Ti} both model linear elastic bones together with linear viscoelastic cartilage layers. To properly capture the distinct material behaviors we have to resolve the bone–cartilage interface with the grids. This problem needs special treatment, because the cartilage layers can be very thin.

In the following we focus on the femur and its cartilage layer only. The tibia is treated analogously, while the fibula, which in our model does not have a cartilage layer, will simply be discretized by a standard simplicial grid.

Let $\Omega_{\text{Fe}} = \Omega_{\text{FeB}} \cup \Omega_{\text{FeC}}$ be the domain of the femur grid and its cartilage layer. We construct a grid for Ω_{Fe} by first building a simplicial conforming grid $\mathcal{G}_{\text{FeB}}$ for Ω_{FeB}. The curved boundaries are approximated by triangular surfaces, and we assume that these surfaces resolve the Dirichlet and Neumann boundaries.

The grid $\mathcal{G}_{\text{FeB}}$ induces a two-dimensional simplicial trace grid $\mathcal{G}_{\Gamma_{\text{Fe}}}$ on the bone–cartilage interface Γ_{Fe}. To construct a grid for the cartilage domain Ω_{FeC}, we first compute the average outer normals of Γ_{Fe} at the vertices of $\mathcal{G}_{\text{Fe}}$. We then create a copy of $\mathcal{G}_{\Gamma_{\text{Fe}}}$ by moving it along the normals onto the outer boundary of Ω_{FeC}. The two two-dimensional grids are connected by edges along the normal direction. The result is a three-dimensional grid for the cartilage layer, consisting of a single layer of prism elements (Figure 4.1, and Figure 4.2, left).

Remark 4.1. It is still a difficult problem to properly segment cartilage layers from medical images, and hence to obtain accurate geometries for the cartilage layers Ω_{FeC} and Ω_{TiC}. It is easier to work with a cartilage layer thickness function, which may be measured or taken from the literature. Then, algorithmically, the cartilage domains (and not just the grids) are constructed by the above procedure, using the layer thickness to construct the outer copy of $\mathcal{G}_{\Gamma_{\text{Fe}}}$.

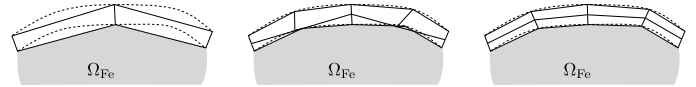The grids thus constructed should be fairly coarse, because for a good multigrid hierarchy we want to perform several steps of uniform and/or adaptive refinement to obtain the grids used to actually discretize the PDEs. Creating the final grids by successive steps of refinement of a coarse grid leads to problems with the boundary approximation, however. Bone geometry taken from medical image data is usually available in much more detail than what can be resolved by the coarsest grid. To keep all the geometric information we use the simplification algorithm described in [31] to obtain boundary parametrizations. These are then used to move new boundary vertices created during refinement onto the original high-resolution surface obtained from image segmentation. The result is a piecewise linear grid boundary that approaches a high-resolution boundary as it is refined.

While the use of parametrized boundaries leads to big improvements in the approximation of the geometry, it also leads to problems with the mesh quality. In particular, the grids of the thin cartilage layers get corrupted easily when displacing vertices on the cartilage boundary (Figure 4.2). To cope with the situation we have implemented the following grid improvement algorithm. First note that we have a boundary parametrization only on the grid–cartilage interface (see Remark 4.1). We first create a properly scaled copy of this parametrization on the opposite boundary of the cartilage layer. This will make the cartilage boundaries "move in parallel" during refinement. To preserve the quality of the grid elements we use the prism structure of the cartilage grid. Since the grid vertices form columns over boundary vertices of the bone grid, we can reposition all cartilage inner vertices to be at uniform distances within their respective columns. This restores the grid quality from before the refinement step (Figure 4.2, right).

After this rather involved treatment of the grids, the actual discretization of the continuum mechanics equations (3.1) is straightforward. For each of the three grids $\mathcal{G}_{\text{Fe}} = \mathcal{G}_{\text{FeB}} \cup \mathcal{G}_{\text{FeC}}$, $\mathcal{G}_{\text{Ti}} = \mathcal{G}_{\text{TiB}} \cup \mathcal{G}_{\text{TiC}}$, and $\mathcal{G}_{\text{Fi}}$ we use the first-order Lagrange space $\mathbf{S}_h$ on that grid. If Dirichlet conditions are prescribed we denote by $\mathbf{S}_{h,D}$ the affine subspace of $\mathbf{S}_h$ that fulfills these conditions.

4.2 Mortar Elements for Cartilage–Cartilage Contact

The discretization of the continuum problems is complicated by the nonpenetration condition (2.4). It is well known that a straightforward pointwise discretization

will lead to instabilities. Instead, mortar methods fulfill optimal discretization error bounds and produce very satisfying results in practice [57,35]. Mortar methods for contact problems have been described in detail elsewhere [58]. Here we only revisit them briefly for comprehensiveness.

Remember from Section 2.1 that we modeled the nonpenetration of the femur and tibia bones and corresponding cartilage layers by conditions on the coupling boundaries $\Gamma_{\text{Fe,C}}$ and $\Gamma_{\text{Ti,C}}$. These were identified by a homeomorphism $\boldsymbol{\phi} : \Gamma_{\text{Fe,C}} \to \Gamma_{\text{Ti,C}}$, and the relative normal displacement $[\cdot]_{\boldsymbol{\phi}}$ was defined in (2.3). Nonpenetration was then modeled by requiring that $[\mathbf{u} \cdot \boldsymbol{\nu}]_{\boldsymbol{\phi}} < g$, where $g : \Gamma_{\text{Fe,C}} \to \mathbb{R}$ was a reference gap function.

The idea of the mortar method is to enforce the nonpenetration constraint in a weak form

$$\int_{\Gamma_{\text{Fe,C}}} [\mathbf{u} \cdot \boldsymbol{\nu}]_{\boldsymbol{\phi}} \mu \, ds \leq \int_{\Gamma_{\text{Fe,C}}} g\mu \, ds \quad \forall \mu \in M, \qquad (4.1)$$

where the mortar space M is defined by

$$M := \left\{ \mu \in H^{-1/2}(\Gamma_{\text{Fe,C}}) \,\Big|\, \int_{\Gamma_{\text{Fe,C}}} \mu v \, ds \geq 0 \right.$$
$$\left. \forall \, v \in H^{1/2}(\Gamma_{\text{Fe,C}})^+ \right\},$$

and $H^{1/2}(\Gamma_{\text{Fe,C}})^+$ denotes the space of all traces on $\Gamma_{\text{Fe,C}}$ that are positive almost everywhere.

We first discretize the geometric objects in (4.1). A continuous discrete outer unit normal field $\boldsymbol{\nu}_h$ can be constructed by averaging over the incident triangle normals to obtain vertex normals and then extending those linearly on the boundary triangles. The discrete contact mapping $\boldsymbol{\phi}_h$ is chosen to be the normal projection of $\Gamma_{\text{Fe,C}}$ onto $\Gamma_{\text{Ti,C}}$. Details on the efficient implementation of such piecewise affine homeomorphisms can be found in [43,46].

Finally, we discretize the mortar space M. We use dual mortar basis functions for the discretization of the mortar space as proposed in [56]. These piecewise linear functions are discontinuous and fulfill the following biorthogonality relation: Let T be a simplex, and let θ_q and ψ_p denote the dual and nodal basis function of the corners $p, q \in T$, then

$$\int_T \theta_q \psi_p dx = \delta_{pq} \int_T \psi_p \, dx. \qquad (4.2)$$

The discrete mortar space M_h is the positive cone spanned by the biorthogonal basis functions θ

$$M_h := \left\{ \mu_h \in \operatorname*{span}_{p \in \Gamma_{\text{Fe,C}}} \theta_p \,\Big|\, \int_{\Gamma_{\text{Fe,C}}} \mu_h v_h \, ds \geq 0 \right.$$
$$\left. \forall v_h \in S_h(\Gamma_{\text{Fe,C}})^+ \right\},$$

where $S_h(\Gamma_{\text{Fe,C}})^+$ is the space of all first-order Lagrangian finite element functions on $\Gamma_{\text{Fe,C}}$ with positive coefficients. On the discretized domains, the weak contact

constraints therefore read

$$\int_{\Gamma_{\text{Fe,C}}} [\mathbf{v}_h \cdot \boldsymbol{\nu}_h]_{\boldsymbol{\phi}_h} \mu_h \, ds \leq \int_{\Gamma_{\text{Fe,C}}} g_h \mu_h \, ds \quad \forall \mu_h \in M_h, \qquad (4.3)$$

with a suitable approximation g_h of the reference gap function g. Consequently, we obtain the set of discrete weakly admissible displacements

$$\mathcal{K}_h := \left\{ \mathbf{v}_h \in \mathbf{S}_{h,D} \,\Big|\, \int_{\Gamma_{\text{Fe,C}}} [\mathbf{v}_h \cdot \boldsymbol{\nu}_h]_{\boldsymbol{\phi}_h} \mu_h \, ds \leq \int_{\Gamma_{\text{Fe,C}}} g_h \mu_h \, ds \right.$$
$$\left. \forall \mu_h \in M_h \right\}.$$

Overall, the discrete spatial problem of the contact-stabilized Newmark integrator then is: Given displacements $\mathbf{u}_h^n$ and velocities $\dot{\mathbf{u}}_h^n$ at time step n, find displacements $\mathbf{u}_{h,\text{pred}}^{n+1}$, $\mathbf{u}_h^{n+1}$ and velocities $\dot{\mathbf{u}}_h^{n+1}$ such that

$$0 \in \mathbf{u}_{h,\text{pred}}^{n+1} - \left(\mathbf{u}_h^n + \tau \dot{\mathbf{u}}_h^n \right) + \partial I_{\mathcal{K}_h} \left(\mathbf{u}_{h,\text{pred}}^{n+1} \right) \quad (4.4a)$$

$$0 \in \mathbf{u}_h^{n+1} - \mathbf{u}_{h,\text{pred}}^{n+1} + \frac{\tau^2}{2} \left(\mathbf{F} \left(\frac{\mathbf{u}_h^n + \mathbf{u}_h^{n+1}}{2} \right) \right.$$
$$\left. + \mathbf{G} \left(\frac{\mathbf{u}_h^{n+1} - \mathbf{u}_h^n}{\tau} \right) + \partial I_{\mathcal{K}_h} \left(\mathbf{u}_h^{n+1} \right) \right) \qquad (4.4b)$$

$$\dot{\mathbf{u}}_h^{n+1} = \frac{\mathbf{u}_{h,\text{pred}}^{n+1} - \mathbf{u}_h^n}{\tau} - \tau \left(\mathbf{F} \left(\frac{\mathbf{u}_h^n + \mathbf{u}_h^{n+1}}{2} \right) \right.$$
$$\left. + \mathbf{G} \left(\frac{\mathbf{u}_h^{n+1} - \mathbf{u}_h^n}{\tau} \right) - \mathbf{F}_{\text{con}} \left(\mathbf{u}_h^{n+1} \right) \right). \qquad (4.4c)$$

Remark 4.2. Note again that we can intersect $\mathcal{K}_h$ with more sets of similar construction, to model further contact conditions or rigid couplings.

4.3 Geodesic Finite Elements for Cosserat Rods

The last ingredient is the space discretization of the weak spatial Cosserat rod problem (3.11). Our discretization differs from the one given by Simo et al. [50]. In particular, it is much simpler and does not involve history variables.

To discretize the weak formulation (3.11), we need finite-dimensional approximations for two spaces. Let $[0, l]$ be the domain of a Cosserat rod. Both the solution function and the test functions of (3.11) live in the linear space $Y = H^1([0, l], \mathbb{R}^3 \times \mathfrak{so}(3))$. However, for the evaluation of the integrals in the two forms 'dyn' (3.9) and 'pot' (3.10) we also need discrete approximations of the current rod configuration $\boldsymbol{\varphi}^n : [0, l] \to \mathbb{R}^3 \times SO(3)$.

Let $\mathcal{G}$ be a grid of $[0, l]$, i.e., a set of points $0 = s_0 < s_1 < \cdots < s_n = l$. The elements of $\mathcal{G}$ are the intervals $[s_{i+1}, s_i]$, $i = 1, \dots, n - 1$. Discretizing the test function space Y is straightforward, since Y is a linear space. We use the space of first-order finite elements

$$Y_h = \left\{ (\boldsymbol{\eta}_h, \hat{\boldsymbol{\mu}}_h) \in C([0, l], \mathbb{R}^3 \times \mathfrak{so}(3)) \,\Big| \right.$$
$$\left. (\boldsymbol{\eta}_h, \hat{\boldsymbol{\mu}}_h) \text{ linear on each } [s_{i+1}, s_i] \right\}.$$

Discretizing the space Q of rod configurations is more challenging, because the space is nonlinear. Indeed, it

has the structure of a nonlinear manifold. For the discretization of such spaces, geodesic finite elements have been introduced in [45].

Definition 4.1 (Geodesic finite elements). *Let $\mathcal{G}$ be a grid on $[0, l]$ and M a Riemannian manifold. We call $\boldsymbol{\varphi}_h : [0, l] \to M$ a geodesic finite element function for M if it is continuous and, for each element $[s_i, s_{i+1}]$ of $\mathcal{G}$, $\boldsymbol{\varphi}_h|_{[s_i, s_{i+1}]}$ is a minimizing geodesic on M.*

Geodesic finite elements for a manifold M are conforming in the sense that they are contained in the Sobolev space $H^1([0, l], M)$. For $M = \mathbb{R}^3 \times SO(3)$, the interpolation along geodesics, along with the necessary derivatives, can be evaluated explicitly. Details are given in [45].

Using the new finite element spaces we can state the discrete problem. Let $V_h^{SE(3)}$ be the space of first-order $SE(3)$-valued geodesic finite elements with respect to $\mathcal{G}$, and let $\boldsymbol{\varphi}_h^n \in V_h^{SE(3)}$ be the discrete rod configuration at time step n. The spatial discrete rod problem is then to find an increment $(\boldsymbol{\delta}_h, \boldsymbol{\theta}_h) \in Y_h$ such that

$$\frac{1}{\tau} \mathrm{dyn}_{\boldsymbol{\varphi}_h^n}[(\boldsymbol{\delta}_h, \boldsymbol{\theta}_h); (\boldsymbol{\eta}_h, \boldsymbol{\mu}_h)] + \mathrm{pot}_{\boldsymbol{\varphi}_h^n}[(\boldsymbol{\delta}_h, \boldsymbol{\theta}_h); (\boldsymbol{\eta}_h, \boldsymbol{\mu}_h)]$$
$$= -\int_0^l A_\rho g \mathbf{z} \boldsymbol{\eta}_h \, ds \tag{4.5}$$

for all test functions $(\boldsymbol{\eta}_h, \boldsymbol{\mu}_h) \in Y_h$. This problem is well-defined, because $V_h^{SE(3)} \subset H^1([0, l], SE(3))$. Note that the discretization retains all invariance properties contained in the continuous model [45, Lem. 4.4].

5 Domain Decomposition Solvers

We have seen that after time discretization the spatial problem of the heterogeneous model consists of the variational inclusions (4.4) for the bone–cartilage compounds, and variational equations (4.5) for each Cosserat rod. These problems are coupled by the contact condition (4.3), and the bone–ligament coupling conditions (2.12)–(2.14). We now first present a domain decomposition algorithm that solves the overall problem. Then we briefly comment on how to solve the subdomain problems.

5.1 Dirichlet–Neumann Algorithm for the Bone–Ligament System

The algorithm used to solve the coupled spatial bone–ligament problems is based on a Steklov–Poincaré formulation. This means that we view only the interface configurations as the independent variables, and we use an iterative method to find the correct values for these interface variables. The overall solution then follows from solving individual subdomain problems with the interface variables as boundary conditions [42].

Since the bone–ligament coupling involves two different types of models there is some choice for the interface variables. We pick the configurations of the rods at their terminal cross sections. For each ligament L $\in$ {ACL, MCL, PCL, LCL} let $\lambda_{L,\mathrm{prox}}, \lambda_{L,\mathrm{dist}} \in SE(3)$ denote the configurations of the proximal and the distal end, respectively. The Dirichlet–Neumann algorithm can then be interpreted as a fixed-point iteration for the set of $\lambda_{L,\mathrm{prox}}, \lambda_{L,\mathrm{dist}}$, L $\in$ {ACL, MCL, PCL, LCL} in the space $SE(3)^8$, the eight-fold Cartesian product of $SE(3)$.

Each iteration of the Dirichlet–Neumann loop consists of three steps: a Dirichlet problem for each of the rods, a contact problem for the three bones and cartilage, with Neumann conditions at the coupling boundaries, and a damped update along geodesics on $SE(3)^8$. For each L, let $\lambda_{L,\mathrm{prox}}^0, \lambda_{L,\mathrm{dist}}^0 \in SE(3)$ be the initial interface values, $k \geq 0$ the Dirichlet–Neumann iteration number and n the time step number. In more detail, the steps are as follows.

1. *Dirichlet problems for the Cosserat rods*
Let $\lambda_{L,\mathrm{prox}}^k, \lambda_{L,\mathrm{dist}}^k \in SE(3)$, L $\in$ {ACL, MCL, PCL, LCL} be the current interface values. For each of the rods L solve the problem

$$\frac{1}{\tau} \mathrm{dyn}_{\boldsymbol{\varphi}_{L,h}^n} \left[(\boldsymbol{\delta}_{L,h}^{n,k+1}, \boldsymbol{\theta}_{L,h}^{n,k+1}); (\boldsymbol{\eta}_h, \boldsymbol{\mu}_h) \right]$$
$$+ \mathrm{pot}_{\boldsymbol{\varphi}_{L,h}^n} \left[(\boldsymbol{\delta}_{L,h}^{n,k+1}, \boldsymbol{\theta}_{L,h}^{n,k+1}); (\boldsymbol{\eta}_h, \boldsymbol{\mu}_h) \right] = -\int_0^{l_L} A_\rho g \mathbf{z} \boldsymbol{\eta}_h \, ds \tag{5.1}$$

for all test function

$$(\boldsymbol{\eta}_h, \hat{\boldsymbol{\mu}}_h) \in Y_{L;h,0} := \{ y_h \in Y_{L;h} \mid y_h(0) = y_h(l_L) = 0 \}$$

with Dirichlet boundary conditions

$$\boldsymbol{\delta}_{L,h}^{n,k+1}(0) = (\lambda_{L,\mathrm{prox}}^k)_{\mathbf{r}} - \mathbf{r}_{L,h}^n(0)$$

and

$$\boldsymbol{\theta}_{L,h}^{n,k+1}(0) = \mathrm{cay}^{-1} \left[(\lambda_{L,\mathrm{prox}}^k)_R \cdot (R_{L,h}^n(0))^{-1} \right],$$

and analogously for $\boldsymbol{\delta}_{L,h}^{n,k+1}(l_L)$ and $\boldsymbol{\theta}_{L,h}^{n,k+1}(l_L)$ coupling with $\lambda_{L,\mathrm{dist}}^k$. We have used $(\lambda_{L,\mathrm{prox}}^k)_{\mathbf{r}}$ and $(\lambda_{L,\mathrm{prox}}^k)_R$ to denote the translational and rotational parts of $\lambda_{L,\mathrm{prox}}^k \in SE(3)$. The definition of the inverse Cayley transform is given in (3.6). The boundary conditions are chosen such that after applying the energy–momentum update formulas (3.8) we get

$$\boldsymbol{\varphi}_{L,h}^{n,k+1}(0) = \lambda_{L,\mathrm{prox}}^k \qquad \text{and} \qquad \boldsymbol{\varphi}_{L,h}^{n,k+1}(l_L) = \lambda_{L,\mathrm{dist}}^k.$$

2. *Neumann problems for the continua*
The new rod iterates $\boldsymbol{\varphi}_{L,h}^{n,k+1}$ exert resultant forces and moments across their proximal and distal cross-sections onto the bones. Let L be one of the rods, and let $\Gamma_{\mathrm{Fe},L}$ be the coupling boundary corresponding to its proximal end on the femur boundary. The resultant forces and moments are $\mathbf{n}_L^{n,k+1}(0)\boldsymbol{\nu}_{L,\mathrm{prox}}$ and $\mathbf{m}_L^{n,k+1}(0)\boldsymbol{\nu}_{L,\mathrm{prox}}$. The construction for the distal ligament ends proceeds analogously. To be able to apply these resultant forces and moments as a boundary condition on the continuum we

construct a Neumann data field $\boldsymbol{\tau}_{\mathrm{Fe,L}}^{k+1} : \Gamma_{\mathrm{Fe,L}} \to \mathbb{R}^3$ such that

$$\int_{\Gamma_{\mathrm{Fe,L}}} \boldsymbol{\tau}_{\mathrm{Fe,L}}^{k+1}\, dx = -\mathbf{n}_{\mathrm{L}}^{n,k+1}(0)\boldsymbol{\nu}_{\mathrm{L,prox}}$$

and

$$\int_{\Gamma_{\mathrm{Fe,L}}} (x - \mathbf{r}_{\mathrm{L},h}^{n,k+1}(0)) \times \boldsymbol{\tau}_{\mathrm{Fe,L}}^{k+1}(x)\, dx = -\mathbf{m}_{\mathrm{L}}^{n,k+1}(0)\boldsymbol{\nu}_{\mathrm{L,prox}}.$$

These are just the dual coupling conditions (2.14). The fields $\boldsymbol{\tau}_{\mathrm{Fe,L}}^{k+1}$ are constructed to be "as constant as possible", by solving small constrained minimization problems (see [43,47] for details).

We construct Neumann data fields $\boldsymbol{\tau}_{\mathrm{Fe}}$, $\boldsymbol{\tau}_{\mathrm{Ti}}$, $\boldsymbol{\tau}_{\mathrm{Fi}}$ for the femur, tibia, and fibula bones by superposition of the separate Neumann fields for the individual rods. With the Neumann data fields available, we solve the three-dimensional linear elastic contact problem (4.4) for resulting new displacements $\mathbf{u}_h^{n,k+1}$ and velocities $\dot{\mathbf{u}}_h^{n,k+1}$, with Neumann data $\boldsymbol{\tau}_{\mathrm{Fe}}$, $\boldsymbol{\tau}_{\mathrm{Ti}}$, $\boldsymbol{\tau}_{\mathrm{Fi}}$.

3. *Damped geodesic update*

From the configuration $\mathbf{u}_h^{n,k+1}$ of the bones and cartilage computed in the previous step we can compute average displacements and orientations of the coupling boundaries. Let Γ be any one of the ligament insertion patches. Using the primal coupling conditions (2.12) and (2.13) we compute the average interface displacement and orientation

$$\mathrm{Av}_\Gamma(\mathbf{u}_h^{n,k+1}) :=$$
$$\left(\frac{1}{|\Gamma|} \int_\Gamma (\mathbf{u}_h^{n,k+1}(x) + x)\, dx, \mathrm{polar}_\Gamma(\mathbf{u}_h^{n,k+1})R_0 \right),$$

where we have used R_0 to denote the reference orientation of the rod at the corresponding end.

It is well known even for the linear case that Dirichlet–Neumann methods will only converge if properly damped [42]. However, the usual damping using an affine combination between old and new iterates cannot be used here, because the interface space is nonlinear. Instead, we damp along geodesics in SE(3). Let $\theta > 0$ be a damping parameter. The new interface values $\lambda_{\mathrm{L}}^{k+1}$ are then computed as geodesic combinations in SE(3) of the old value λ_{L}^k and $\mathrm{Av}_\Gamma(\mathbf{u}_h^{n,k+1})$,

$$\lambda_{\mathrm{L}}^{k+1} = \exp_{\lambda_{\mathrm{L}}^k} \theta \left[\exp_{\lambda_{\mathrm{L}}^k}^{-1} \mathrm{Av}_\Gamma(\mathbf{u}_h^{n,k+1}) \right].$$

Fixed points of the Dirichlet–Neumann iteration solve the coupling conditions (2.12)–(2.14) and the subdomain equations. Given such a fixed point $\Lambda \in \mathrm{SE}(3)^8$ with associated subdomain solutions $\tilde{\mathbf{u}}_h$ and $\tilde{\boldsymbol{\varphi}}_h$, we set

$$\mathbf{u}_h^{n+1} = \tilde{\mathbf{u}}_h \qquad \text{and} \qquad \boldsymbol{\varphi}_h^{n+1} = \tilde{\boldsymbol{\varphi}}_h$$

to obtain the solution of the coupled system at the next time step.

5.2 Subdomain Solvers

The expensive parts of the fixed-point loop of the previous section are the solutions of the different subdomain problems. Of the two, the rod problems are simpler to solve. After choosing a basis for the space Y_h, each rod problem (5.1) becomes a nonlinear algebraic system of equations not associated to a minimization problem. Such a problem can be solved with a standard damped Newton solver. Due to the one-dimensional nature of the rod grids, the Newton matrices have a block-tridiagonal structure. Hence the linear correction problems can be solved directly in linear time using the Thomas algorithm.

Solving the contact problems (4.4) is more involved. We first note that of the three steps, the third one is straightforward, as it does not involve solving an equation. Similarly to the space continuous case treated in Section 3.1, we can show that the other two steps correspond to minimization problems

$$\mathbf{u}_{h,\mathrm{pred}}^{n,k+1} = \arg\min_{\mathbf{v}_h \in \mathcal{K}_h} \frac{1}{2} \left\| \mathbf{v}_h - (\mathbf{u}_h^n + \tau \dot{\mathbf{u}}_h^n) \right\|_{\mathbf{L}_2}^2, \qquad (5.2)$$

and

$$\mathbf{u}_h^{n,k+1} = \arg\min_{\mathbf{v}_h \in \mathcal{K}_h} \left[\frac{1}{2} g(\mathbf{v}_h, \mathbf{v}_h) - \tau^2 f_{\mathrm{ext}}(\mathbf{u}_h^n + \mathbf{v}_h) \right], \quad (5.3)$$

with $g(\cdot, \cdot)$ and f_{ext} given by (3.3) and (2.6), respectively. To efficiently solve the first one we lump the mass matrix occurring in the algebraic formulation of (5.2). Then, (5.2) decouples into individual 3×3 convex quadratic minimization problems with at most one linear inequality constraint each. In this form, (5.2) can be solved exactly with a single block-Jacobi iteration.

The second minimization problem (5.3) involves the energy norm $g(\cdot, \cdot)$. We have shown in [43,18] how the Truncated Nonsmooth Newton Multigrid (TNNMG) method can be used to solve problems with this structure robustly and efficiently. Key ingredient is a special transformation of the finite element basis originally introduced in [58]. In this new basis, the constraints that form the admissible set $\mathcal{K}_h$ decouple and we obtain a set of box constraints. The basis transformation can be constructed cheaply by exploiting the biorthogonality (4.2) of the mortar basis functions. In the transformed basis, the TNNMG method takes the following form:

1. Nonlinear Gauß–Seidel presmoothing,
2. one linear multigrid step restricted to the degrees of freedom not in contact,
3. projection of the correction onto the admissible set,
4. line search.

For strictly convex, quadratic problem, the TNNMG method converges globally:

Theorem 5.1 ([17, Thm. 6.4]). *Let J be a strictly convex, quadratic functional. For any initial iterate, the Truncated Nonsmooth Newton Multigrid algorithm converges to the unique minimizer of J in $\mathcal{K}_h$.*
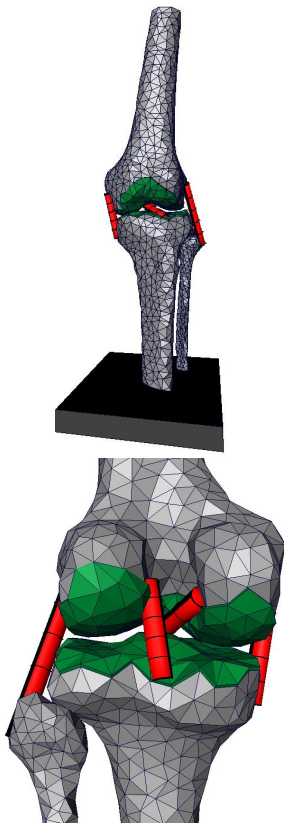
Fig. 6.1. Initial configuration of the numerical experiment

After a finite number of steps the method degenerates to a linear multigrid method, and hence converges with multigrid speed. That finite number of steps is usually very low. A discussion and numerical experiments can be found in [43, 18].

6 Numerical Experiment

In this section we want to demonstrate the performance of the discretizations and solvers numerically. For this we revisit the benchmark problem of [29] with our more elaborate model.

In [29], we considered the motion of a knee model consisting only of proximal femur and distal tibia bones. The model was subjected to an initial constant downward velocity, and made to impact a rigid obstacle. The numerical results of [29] showed how the tibia bone bounces off the obstacle and into the femur. Simulations over longer times were not possible using that model, because the bones, not being attached to each other at all, would fly apart after the first impact. With our improved model this is no longer the case.

Model specification. Geometry data of the femur, tibia, and fibula bones was taken from the Visible Human Data Set [1]. From the segmented image data, high-resolution boundary surfaces of the bones were extracted. These

boundary surfaces were coarsened to a resolution suitable for multigrid coarse grids. Together with the coarsening, we constructed parametrizations of the original boundary surfaces over the coarse surfaces using the algorithm from [31, 46]. From the coarse boundary surfaces, tetrahedral grids were constructed using the Amira[3] grid generator. The resulting grids for femur, tibia, and fibula bone had 3 787, 2 550, and 1 253 elements, respectively. The actual computations were done on a hierarchy of grids obtained by two steps of uniform refinement. The finest grids then had 242 368, 163 200, and 80 192 elements, respectively.

Using data from an anatomy book [41], we manually marked the areas on the femur and tibia covered by articular cartilage. On these areas we then created cartilage layers consisting of prism elements using the construction technique introduced in Section 4.1. We used a constant layer thickness of 1.5 mm [59]. The cartilage grids on the femur and tibia contained 171 and 129 prism elements, respectively. They were also twice uniformly refined, resulting in fine grids of 10 944 and 8 256 prism elements. All in all the bone and cartilage computational grids consisted of 504 960 elements and 105 247 vertices.

Ligament insertion sites were also marked manually using generic data [41]. The initial ligament configurations were defined as in Section 2.3. We did not set a pre-strain, to allow for a more visible movement of the knee joint. Ligaments were modelled as to have a circular cross section with a radius of 5 mm. Each ligament was discretized with a uniform grid with 20 elements.

As in [29], a rigid obstacle was placed 1 mm below tibia and fibula. Mathematically, this obstacle was modelled as an additional pointwise inequality constraint on the vertices at the bottom of the model (cf. Remarks 2.1 and 4.2). A set of weak equality constraints was added to couple the bottom ends of the tibia and fibula together.

The entire initial configuration is illustrated in Figure 6.1. Initially, the entire model moved downward with a constant velocity vector of $(0, 0, -1)$ m/s. Outside of the contact and ligament insertion patches, we assumed homogeneous Neumann boundary conditions everywhere. Additionally, all bones, cartilage, and ligaments were subject to gravity.

Material parameters were taken from the literature. Realistic values for the elasticity parameters of human bones can be found in [11]. Corresponding values for ligaments and articular cartilage have been chosen on the basis of [53] and [14], respectively. Unfortunately, no values for the viscosity parameters of cartilage could be found in the literature; we use the same values as [24]. All material parameters are summarized in Table 6.1.

Algorithmic specification. The implementation of the numerical solvers was based on the Dune libraries[4] [7]. Within Dune, the UG grid manager [6] was used to handle the bone and cartilage grids. The module `dune-grid-glue`

---

[3] `www.amira.com`

[4] `www.dune-project.org`

parameter	symbol	bone	cartilage	ligament
Young's modulus	E	17 GPa	10 MPa	330 MPa
Poisson ratio	ν	0.3	0.4	0.3
shear/bulk viscosity	μ	—	10 MPa·s	—
mass density	ρ	2 g/cm^3	1 g/cm^3	1 g/cm^3

Table 6.1. Material parameters for bone, cartilage, and ligaments

Fig. 6.3. Total energy of the system. Shaded areas denote the phases of contact with the rigid obstacle (left), and of cartilage–cartilage contact (right)

[8] allowed for convenient coupling of the contact boundaries.

We simulated the evolution of the model over a time interval $[0\,\mathrm{s}, 10^{-3}\,\mathrm{s}]$. This is long enough to include both the first impact onto the foundation and the subsequent contact between femur and tibia. We split the interval into 100 time steps. The resulting time step size $\tau = 10^{-5}\,\mathrm{s}$ was small enough such that each contact phase was well resolved.

We set the Dirichlet–Neumann damping parameter θ to 0.6, which has been found to be the optimal value for the corresponding static problem [47]. The Dirichlet–Neumann algorithm was set to iterate until the infinity norms of the relative ligament and bone corrections dropped below 10^{-4}. In each iteration the algebraic contact problem was solved using the TNNMG method with a multigrid $V(3, 3)$-cycle as linear correction. The TNNMG solver was set to iterate until the relative correction was less than 10^{-5} in the energy norm. This was the largest value that could be used without noticeably changing the energy behavior of the overall knee model. The cheap ligament problems were solved up to machine precision with a damped Newton solver.

Numerical findings.   Figure 6.2 illustrates the evolution of the displacements and the distribution of the von Mises stresses in the bones and cartilage at various points in time. The first stresses arise when the fibula and tibia hit the rigid obstacle at time step $n = 11$ and one can observe the resulting shock wave traveling through the lower bones. As the femur approaches the tibia small stresses at the ligament insertion sites emerge ($n = 30$). At time step $n = 48$ first contact of the cartilages occurs, which causes a second shock wave that runs through the femur ($n = 59$). The knee joint separates again at time step $n = 66$. However, as expected, the ligaments keep the joint from coming apart.

Figure 6.3 shows the total energy, including the viscous energy, of the bodies and the ligaments over time. From Theorems 3.3 and 3.5, we expect the system to be energy conserving as long as there are no changes of the contact zone, and dissipative otherwise. We observe that the coupled system is indeed dissipative, and that the vast majority of energy loss occurs during femur–tibia contact. However, we also see a small additional energy loss in the periods without contact, which must be attributed to the coupling. A precise analysis of alternative coupling conditions is the subject of current work [44].
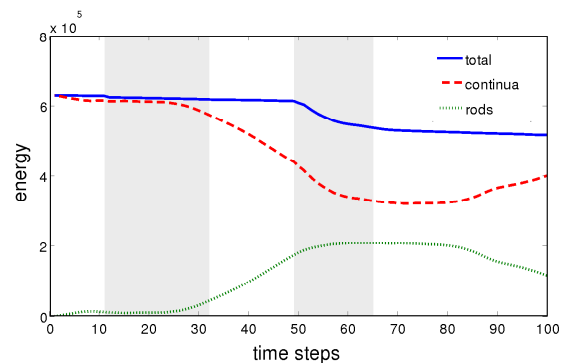
Figure 6.4 presents the number of active contact nodes as a function of time. No numerical oscillations appear (see Figures 2.5–2.7 in [24] for an illustration of these oscillations). Note that the small increase of active nodes at the end of the contact phase with the rigid obstacle is not artificial.

In Figure 6.5, left, the total number of Dirichlet–Neumann iterations per time step is represented. No more than 5 iterations are needed for the required accuracy. This translates to an average convergence rate of 0.12. Figure 6.5, right, shows the average number of iterations for the solution of one contact problem involving the three bones and their cartilage layers. The TNNMG solver shows an excellent average convergence rate of 0.3. During the contact phases with the rigid obstacle and the cartilage the convergence rates rise slightly to an average of 0.35.

The computational time for the solution of the contact problem, again averaged over the Dirichlet–Neumann iterations for each time step, is illustrated in Figure 6.6 together with the overall time for each time step. All computations were done on an Intel Xeon processor clocked at 2.6 GHz. The plots show that the main CPU time is needed for the solution of the contact problems. The excellent performance of the TNNMG enables the solution of these obstacle constrained systems of over 315 000 degrees of freedom in an averaged time of 70 s. The average computation time for the ligament problems is less than 1 s and therefore negligible.

7 Conclusion

We have presented a heterogeneous time-dependent model for the spatially resolved stress analysis of a knee joint. Incorporating articular cartilage and ligaments, it is a definite improvement over our previous model [29]. Together with the model we have proposed discretizations and solution algorithms that were shown to be robust and efficient for this challenging problem.

Nevertheless, many tasks remain. From the modeling point of view, the patella and the two menisci are still missing, and so are muscles and tendons. Moreover,
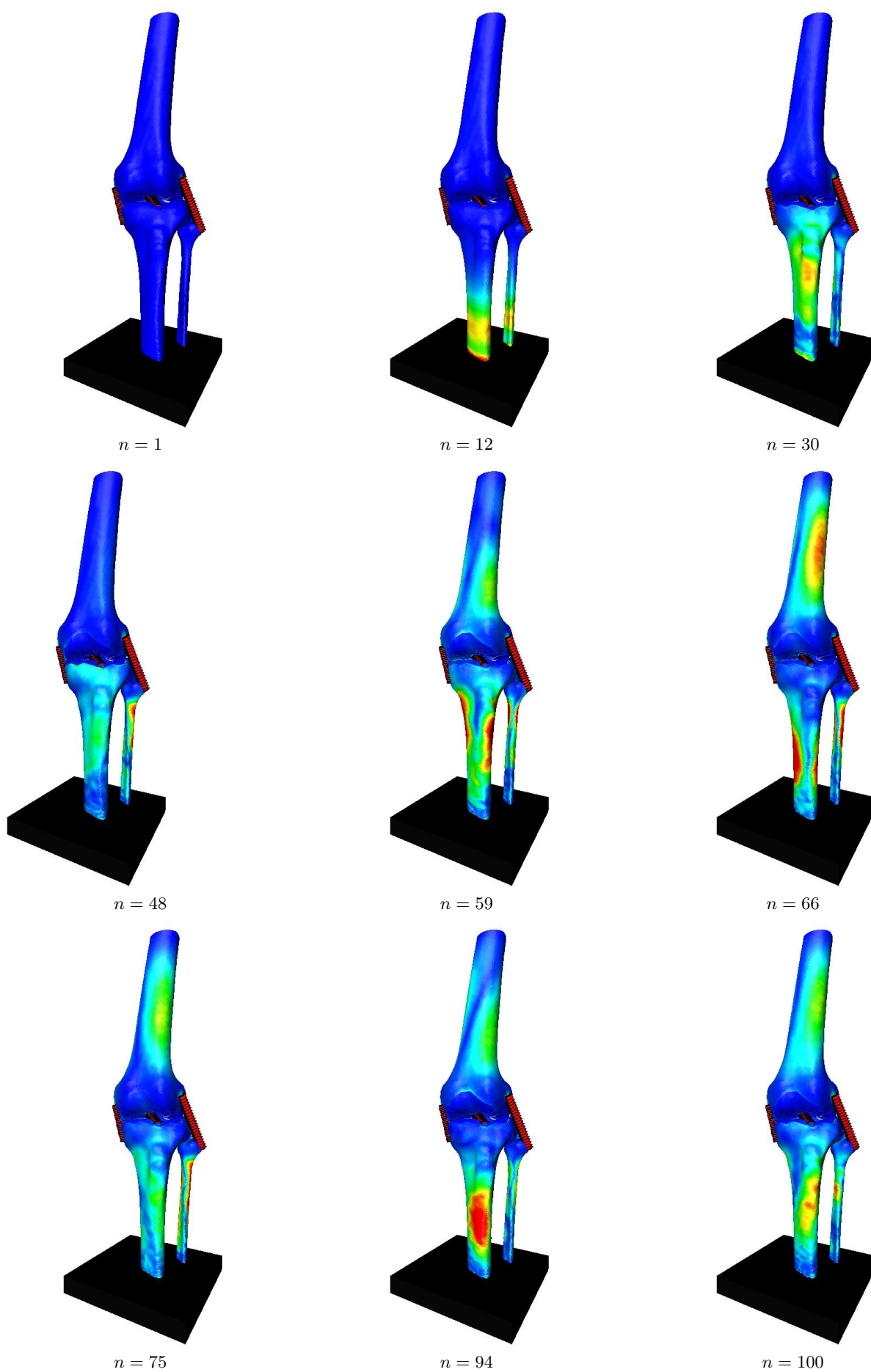
$n = 1$

$n = 12$

$n = 30$

$n = 48$

$n = 59$

$n = 66$

$n = 75$

$n = 94$

$n = 100$

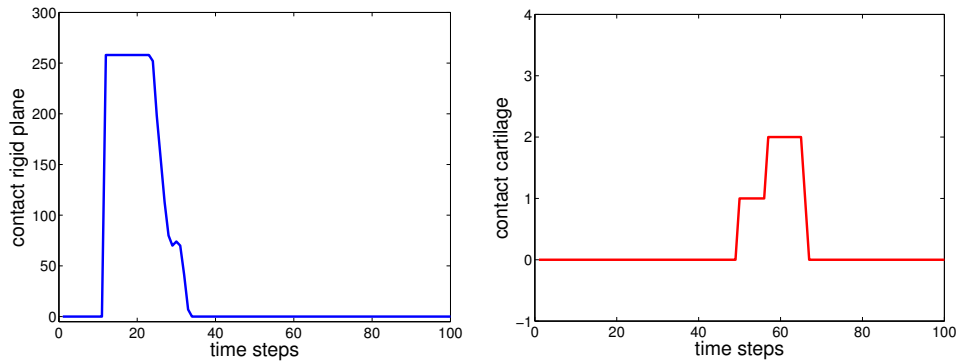**Fig. 6.2.** Time evolution of the spatial distribution of von Mises stresses

Fig. 6.4. Left: Number of contact nodes with rigid plane. Right: Number of contact nodes on the femur cartilage
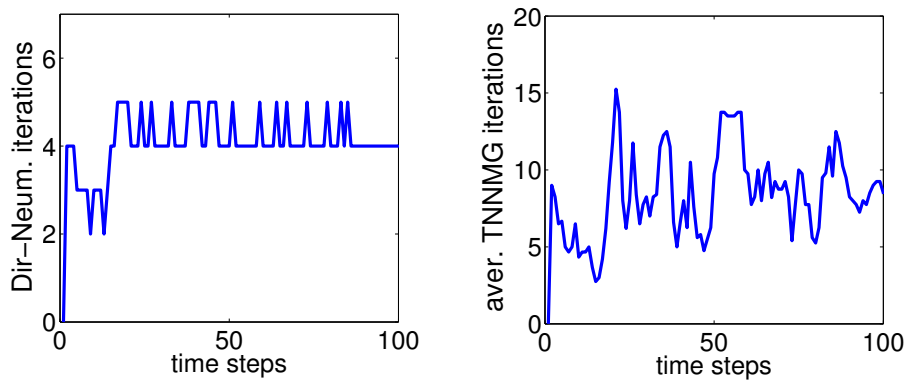

Fig. 6.5. Left: Number of Dirichlet–Neumann iterations per time step. Right: Average number of TNNMG iterations for the contact problem
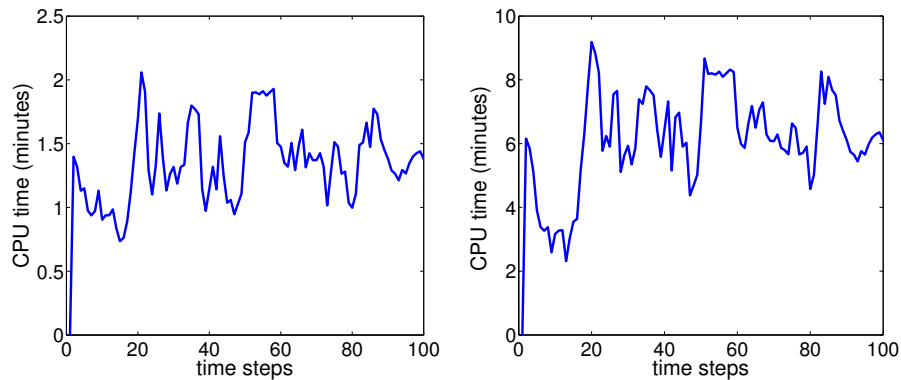

Fig. 6.6. CPU time in minutes. Left: Average time for the solution of one contact problem, plotted for each time step. Right: Overall time per time step.

sooner or later our present linearized viscoelastic cartilage model may have to be replaced by a biphasic model. Simulating actual gait cycles of the knee requires a geometrically nonlinear theory for the bones and cartilage. For this, our Newmark time integrator will have to be extended. CPU times can be lowered significantly using adaptive mesh refinement. Summarizing, there is a lot left to do until a realistic knee model is established that can be used as a basis for surgical decisions.

References

1. The Visible Human Project. `http://www.nlm.nih.gov/research/visible/visible_human.html`.
2. E. Abdel-Rahman and M. S. Hefzy. A two-dimensional dynamic anatomical model of the human knee joint. *J. Biomech. Eng.*, 115:357–365, 1993.
3. J. Ahn and D. E. Stewart. Dynamic frictionless contact in linear viscoelasticity. *IMA J. Numer. Anal.*, 29(1):43–71, 2009.
4. S. S. Antman. *Nonlinear problems of elasticity, volume 107 of Applied Mathematical Sciences*. Springer Verlag, 1991.

5. P. Arbenz, G.H. van Lenthe, U. Mennel1, R. Müller, and M. Sala. A scalable multi-level preconditioner for matrix-free μ-finite element analysis of human bone structures. *Int. J. Numer. Meth. Engrg.*, 73:927 – 947, 1997.

6. P. Bastian, K. Birken, K. Johannsen, S. Lang, N. Neuß, H. Rentz–Reichert, and C. Wieners. UG – a flexible software toolbox for solving partial differential equations. *Comp. Vis. Sci.*, 1:27–40, 1997.

7. P. Bastian, M. Blatt, A. Dedner, C. Engwer, R. Klöfkorn, R. Kornhuber, M. Ohlberger, and O. Sander. A generic interface for adaptive and parallel scientific computing. Part II: implementation and tests in DUNE. *Computing*, 82(2-3):121–138, 2008.

8. P. Bastian, G. Buse, and O. Sander. Infrastructure for the coupling of Dune grids. In *Proc. ENUMATH 2009*, pages 107–114. Springer, 2010.

9. Yanhong Bei and Benjamin J. Fregly. Multibody dynamic simulation of knee contact mechanics. *Med. Eng. Phys.*, 26(9):777–789, 2004.

10. L. Blankevoort and H. Huiskes. Ligament–bone interaction in a three-dimensional model of the knee. *J. Biomech. Eng.*, 113(3):263–269, 1991.

11. J. D. Currey. *Bones: Structure and Mechanics*. Princeton University Press, 2002.

12. P. Deuflhard, R. Krause, and S. Ertel. A contact-stabilized Newmark method for dynamical contact problems. *Internat. J. Numer. Methods Engrg.*, 73(9):1274–1290, 2007.

13. P. Deuflhard and M. Weiser. *Adaptive Numerical Solution of PDEs*. de Gruyter, 2012.

14. T.H. Donahue, M. L. Hull, M. M. Rashid, and C. R. Jacobs. A finite element model of the human knee joint for the study of tibio-femoral contact. *J. Biomech. Eng.*, 124(3):273–280, 2002.

15. C. Eck. *Existenz und Regularität der Lösungen für Kontaktprobleme mit Reibung*. PhD thesis, Universität Stuttgart, 1996.

16. I. Ekeland and R. Temam. *Convex Analysis and Variational Problems*. SIAM, 1987.

17. Carsten Gräser and Ralf Kornhuber. Multigrid methods for obstacle problems. *J. Comp. Math.*, 27(1):1–44, 2009.

18. Carsten Gräser, Uli Sack, and Oliver Sander. Truncated nonsmooth Newton multigrid methods for convex minimization problems. In *Proc. of DD18*, pages 129–136, 2009.

19. E. Hairer, C. Lubich, and G. Wanner. *Geometric Numerical Integration. Structure-Preserving Algorithms for Ordinary Differential Equations.* Springer, 2nd edition, 2006.

20. M. Heller, C. König, H. Graichen, S. Hinterwimmer, R. Ehrig, G. Duda, and W. Taylor. A new model to predict in vivo human knee kinematics under physiological-like muscel activation. *Journal of Biomechanics*, 40:45–53, 2007.

21. C. Huang, V. Mow, and G. Ateshian. The role of flow-independent viscoelasticity in the biphasic tensile and compressive responses of articular cartilage. *J. Biomech. Eng.*, 123(5):410–7, 2001.

22. Stefan Kehrbaum. *Hamiltonian Formulations of the Equilibrium Conditions Governing Elastic Rods: Qualitative Analysis and Effective Properties.* PhD thesis, University of Maryland, 1997.

23. N. Kikuchi and J. T. Oden. *Contact Problems in Elasticity.* SIAM, 1988.

24. C. Klapproth. *Adaptive numerical integration for dynamical contact problems.* PhD thesis, Freie Universität Berlin, 2011. also published at Cuvillier Verl. Göttingen.

25. C. Klapproth, P. Deuflhard, and A. Schiela. A perturbation result for dynamical contact problems. *Numer. Math. Theor. Meth. Appl.*, 2(3):237–257, 2009.

26. C. Klapproth, A. Schiela, and P. Deuflhard. Consistency results on Newmark methods for dynamical contact problems. *Numer. Math.*, 116(1):65–94, 2010.

27. C. Klapproth, A. Schiela, and P. Deuflhard. Adaptive timestep control for the contact-stabilized Newmark method. *Numer. Math.*, 119(1):49–81, 2011.

28. R. Kornhuber and R. Krause. Adaptive multigrid methods for Signorini's problem in linear elasticity. *Comp. Vis. Sci.*, 4(1):9–20, 2001.

29. R. Kornhuber, R. Krause, O. Sander, P. Deuflhard, and S. Ertel. A monotone multigrid solver for two body contact problems in biomechanics. *Comp. Vis. Sci.*, 11(1):3–15, 2008.

30. Ralf Kornhuber. *Adaptive Monotone Multigrid Methods for Nonlinear Variational Problems.* B.G. Teubner, 1997.

31. R. Krause and O. Sander. Automatic construction of boundary parametrizations for geometric multigrid solvers. *Comp. Vis. Sci.*, 9:11–22, 2006.

32. R. Krause, D. Schittler, M. Reiter, S. Waldherr, F. Allgöwer, D. Karastoyanova, F. Leymann, B. Markert, and W. Ehlers. Bone remodelling: A combined biomechanical and systems-biological challenge. *PAMM*, 11:99–100, 2011.

33. W. Lai, J. Hou, and V. Mow. A triphasic theory for the swelling and deformation behaviours of articular cartilage. *J. Biomech. Eng.*, 113:245–58, 1991.

34. T. A. Laursen and V. Chawla. Design of energy conserving algorithms for frictionless dynamic contact problems. *Internat. J. Numer. Methods Engrg.*, 40(5):863–886, 1997.

35. T.A. Laursen. *Computational Contact and Impact Mechanics.* Springer, 2003.

36. M. Machado, P. Flores, J. Claro, J. Ambrósio, M. Silva, A. Completo, and H. Lankarani. Development of a planar multibody model of the human knee joint. *Nonlinear Dynamics*, 60:459–478, 2010.

37. S. G. McLean, A. Su, and A. J. van den Bogert. Development and validation of a 3-D model to predict knee joint loading during dynamic movement. *J. Biomech. Eng.*, 125:864–875, 2003.

38. Udo Nackenhorst. Computational methods for studies on the biomechanics of bones. *Foundations of Civil and Environmental Engineering*, 11:99–100, 2006.

39. M. T. Penrose, G. M. Holt, M. Beaugonin, and D.R. Hose. Development of an accurate three-dimensional finite element knee model. *Comp. Meth. Biomech. Biomed. Eng.*, 5(4):291–300, 2002.

40. S. J. Piazza and S. L. Delp. Three-dimensional dynamic simulation of total knee replacement motion during a step-up task. *J. Biomech. Eng.*, 123:599–607, 2001.

41. R. Putz and R. Pabst, editors. *Sobotta – Atlas der Anatomie des Menschen.* Urban & Fischer, 2000.

42. A. Quarteroni and A. Valli. *Domain Decomposition Methods for Partial Differential Equations.* Oxford Science Publications, 1999.

43. O. Sander. *Multidimensional Coupling in a Human Knee Model.* PhD thesis, Freie Universität Berlin, 2008.

44. O. Sander and A. Schiela. Energy minimizers of the coupling of a Cosserat rod to an elastic continuum. Technical Report 903, Matheon, 2012. submitted.
45. Oliver Sander. Geodesic finite elements for Cosserat rods. *Internat. J. Numer. Methods Engrg.*, 82(13):1645–1670, 2010.
46. Oliver Sander. The psurface library. Technical Report 708, Matheon, 2010. To appear in CVS.
47. Oliver Sander. Coupling geometrically exact Cosserat rods and linear elastic continua. Technical Report 772, Matheon, 2011. To appear in Proc. DD20.
48. E. Schechter. *Handbook of Analysis and its Foundations.* Academic Press, San Diego, 1997.
49. J.C. Simo and N. Tarnow. The discrete energy–momentum method. Conserving algorithms for nonlinear elastodynamics. *J. Appl. Math. Phys.*, 43:757–792, 1992.
50. J.C. Simo, N. Tarnow, and M. Doblaré. Non-linear dynamics of three-dimensional rods: Exact energy and momentum conserving algorithms. *Internat. J. Numer. Methods Engrg.*, 38:1431–1473, 1995.
51. J. Suh and R. Spilker. Indentation analysis of biphasic articular cartilage: nonlinear phenomena under finite deformation. *J. Biomech. Eng.*, 116(1):1–9, 1994.
52. T. M. van Eijden, E. Kouwenhoven, J. Verburg, and W. A. Weijs. A mathematical model of the patellofemoral joint. *J. Biomech.*, 19:219–229, 1986.
53. J. Weiss and J. C. Gardiner. Computational modelling of ligament mechanics. *Critical Reviews in Biomedical Engineering*, 29(4):1–70, 2001.
54. W. Wilson, C. van Donkelaar, R. van Rietbergen, and R. Huiskes. The role of computational models in the search for the mechanical behaviour and damage mechanisms of articular cartilage. *Med. Eng. Ph.*, 27:810–826, 2005.
55. W. Wilson, C. van Donkelaar, R. van Rietbergen, K. Ito, and R. Huiskes. Stresses in the local collagen network of articular cartilage: a poroviscoelastic fibril-reinforced finite element study. *J. Biomech. Eng.*, 37(3):357–66, 2004.
56. B. Wohlmuth. *Discretization Methods and Iterative Solvers based on Domain Decomposition.* LNCSE vol. 17. Springer Verlag, 2001.
57. B. Wohlmuth. Variationally consistent discretization schemes and numerical algorithms for contact problems. *Acta Numerica*, 20:569–734, 2011.
58. B. Wohlmuth and R. Krause. Monotone methods on nonmatching grids for nonlinear contact problems. *SIAM J. Sci. Comput.*, 25(1):324–347, 2003.
59. J. Yao, A. D. Salo, J. Lee, and A. L. Lerner. Sensitivity of tibio–menisco–femoral joint contact behavior to variations in knee kinematics. *J. Biomech. Eng.*, 41(2):390–398, 2008.